Isentropic Analysis on the Intensification of Hurricane Edouard (2014)

Juan Fang

Key Laboratory for Mesoscale Severe Weather, Ministry of Education, and School of Atmospheric Sciences, Nanjing University, Nanjing, China

Olivier Pauluis

Courant Institute of Mathematical Sciences, New York University, New York, New York

Fuqing Zhang

Department of Meteorology, The Pennsylvania State University, University Park, Pennsylvania

ABSTRACT

An isentropic analysis technique is adopted in this study to investigate the intensification of Hurricane Edouard (2014) predicted by an experimental real-time convection-permitting hurricane analysis and forecast system. This technique separates the vertical mass transport in terms of equivalent potential temperature θ_e for the rising air parcels at high entropy from the subsiding air at low entropy. It is found that as Edouard intensifies the vertical circulation becomes wider via the expansion of upward (downward) mass flux to higher (lower) θ_e. In the early developing stages, the asymmetric convection dominates the vertical circulation and leads to a remarkable upward mass flux maximum center in the upper troposphere. When Edouard becomes intense, the axisymmetric convection becomes important to the upper-level vertical mass transport while the asymmetric convection still dominates the low-level vertical mass transport. Development of the warm core in the eye leads to double maxima along the θ_e axis for both the isentropic-mean relative humidity and tangential velocity. The isentropic-mean properties such as the mid- to upper-level relative humidity, vertical velocity, and radial outflow decrease considerably while the mid- to upper-level vorticity enhances on the high-θ_e side before the onset of rapid intensification. The isentropic analysis also reveals that as Edouard intensifies the eye characterized by warm and dry core first forms in the low to middle troposphere and then gradually expands upward. The abovementioned results indicate that the isentropic framework may have the advantages of binning common variables with θ_e that could reflect the changes of the tropical cyclone structure in the inner-core region without a prior specification of the location of the storm center.

1. Introduction

Tropical cyclones (TCs) are warm-core, nonfrontal, low pressure systems that develop over warm oceans (Frank 1977). Their structure and intensity variations have been extensively investigated in the literature (e.g., Smith 1980; Willoughby et al. 1982; Emanuel 1986; Schubert et al. 1999; Houze et al. 2007; Qiu et al. 2010; Qiu and Tan 2013; Fang and Zhang 2010, 2011; Zhang and Chen 2012; Stern and Zhang 2013a,b; Zhang and Tao 2013; Gu et al. 2015; Kieu et al. 2016; Rivoire et al. 2016). Most of the works on TCs are performed in the physical space using the Cartesian coordinates x, y, and z. To gain a different perspective of the physical processes leading to TC intensification, some studies used the potential radius R [where $(1/2)fR^2 = rv + (1/2)fr^2$, with Coriolis parameter f and meridional velocity v] as one of the dependent variables while the actual radius r is treated as one of the independent variables. For example, Schubert and Hack (1983) derived a simpler form of Eliassen's balanced vortex model in the R–z space and found that the transverse circulation equation in the transformed coordinates naturally leads to a new definition of the Rossby radius of deformation—an important dynamical measure for TC development. A similar definition of R in the transformed coordinates was also used by Emanuel (1997) to discuss the TC inner-core dynamics and energetics.

Corresponding author: Dr. Juan Fang, fangjuan@nju.edu.cn

Besides the R–z space, the isentropic coordinates proposed by Rossby (1937) taking potential temperature as the dependent variable in the vertical direction are also used in the studies on TC dynamics. Anthes (1971) developed a diagnostic axisymmetric model in the isentropic coordinates to investigate the effect of different heating on the dynamics and energetics of steady-state TC. Schubert and Alworth (1987) adopted the isentropic coordinates to discuss the influence of latent heat release on TC potential vorticity. Molinari et al. (1995, 1997) investigated the eastern Pacific tropical cyclogenesis and the external influences on TC intensity via analyzing the isentropic potential vorticity. Merrill and Velden (1996) employed the isentropic coordinate analyses of rawinsondes and cloud motion wind vectors to describe the upper-tropospheric and lower-stratospheric circulation associated with Supertyphoon Flo (1990).

More recently, the isentropic analysis has been applied to study various atmospheric flows using the equivalent potential temperature θ_e rather than potential temperature. This is motivated by the fact that the equivalent potential temperature is an adiabatic invariant in the presence of water phase transition, while the potential temperature is not. Pauluis et al. (2008, 2010) have shown that the meridional mass transport increases by a factor of 2 when averaged on surfaces of constant equivalent potential temperature rather than on surfaces of constant potential temperature. Pauluis and Mrowiec (2013, hereafter PM13) introduces the concept of isentropic analysis for convective motions in which θ_e is used to replace the horizontal coordinates. The PM13 technique uses the equivalent potential temperature to replace both horizontal coordinates x and y by sorting air parcels at different altitude z in terms of their θ_e. Via averaging the flow properties at a constant value of θ_e, a comprehensive description of the convective motions can be achieved in the thermodynamic space θ_e–z. Major advantages of this new approach over the conventional isentropic analysis include the following: 1) θ_e is an adiabatic invariant for reversible phase transition and thus is more appropriate to describe the thermodynamic features of a TC accompanied by massive moist convection and 2) the conditional averaging overcomes the limitation of extremely complex geometry of isentropes and low-level unstable stratification. Mrowiec et al. (2016) implemented this technique to analyze the overturning in the mature stage of an idealized hurricane simulated in Fang and Zhang (2012). They found that the isentropic circulation has a maximum in the mass transport near the surface, which is associated with shallow convection and entrainment, while the ascent in the eyewall can be readily identified as an upward mass flux of air with unusually high θ_e. Moreover, Mrowiec et al. (2016) argued that the mass transport in the isentropic circulation is much larger than that calculated in the conventional Eulerian secondary circulation, which underestimates the mass transport by convection in the outer rainbands.

While the isentropic analysis focuses on reconstructing the circulation on isentropic surfaces, recent studies such as Kjellsson et al. (2014), Laliberté et al. (2015), and Pauluis (2016) have introduced new methodology to extract the circulation in multiple thermodynamic coordinates such as entropy and temperature. Riemer and Laliberté (2015) applied a similar technique by averaging Lagrangian trajectories using θ_e and temperature coordinates to study the impact of shear on mixing and entrainment near the eyewall of a hurricane. Via tracing air parcels along the isentropic overturning circulation following a well-defined set of thermodynamic transformations, Pauluis (2016) demonstrated that this new isentropic analysis method can be applied to the study of thermodynamic cycles of various turbulent atmospheric flows. Based on this, Pauluis and Zhang (2017) pointed out that convection in the outer rainbands is inefficient at producing kinetic energy while the deepest overturning circulation associated with the rising air within the eyewall is an efficient heat engine that produces about 70% as much kinetic energy as a comparable Carnot cycle. Altogether, these new approaches that rely on assessing atmospheric flows in the thermodynamic spaces have been shown to provide new insights on the complex interplay between the dynamics and thermodynamics in various meteorological phenomena.

With the intention to obtain an integral description on the evolution of dynamic and thermodynamic structures of an intensifying TC in the isentropic framework, the present study extends the work of Mrowiec et al. (2016) to analyze a state-of-the-art simulation of a TC, Hurricane Edouard (2014), from its formation to rapid intensification. The remainder of this paper is organized as follows. Section 2 is a brief overview of the observed and simulated Edouard. Section 3 presents the isentropic analysis on the simulated Edouard. Concluding remarks are given in section 4.

2. An overview of Edouard and the associated numerical simulation

Edouard originated from an easterly wave that appeared near the African coast on 6 September 2014 (Stewart 2014). By 10 September, convection began to enhance and organize near the surface center in the easterly wave and led to the formation of a named tropical depression by 1200 UTC 11 September. Thereafter, Edouard moved northwestward and intensified gradually. At 1200 UTC 14 September, Edouard was upgraded

to a hurricane and finally developed into the first major hurricane in the Atlantic since Hurricane Sandy (2012) early on 16 September. With a well-defined eye surrounded by intense eyewall convection, Edouard experienced an intensification with the maximum 10-m sustained winds increased by 25 kt ($1 \text{ kt} = 0.51 \text{ m s}^{-1}$) over the period from about 0000 UTC 14 September to 0000 UTC 15 September. Though such an intensifying rate does not meet the traditional criterion for rapid intensification, we look at rapid intensification timing in this work as it is traditionally defined following Munsell et al. (2017) for simplicity.

In this study, the isentropic analysis is carried out on the simulation (prediction) of Edouard produced by the Weather Research and Forecasting (WRF) Model, version 3.5.1 (Skamarock and Klemp 2008), which was a real-time forecast generated by The Pennsylvania State University (PSU) real-time Atlantic hurricane forecast and analysis system (Zhang et al. 2009, 2011; Zhang and Weng 2015; Weng and Zhang 2016). The model domain is triply nested through two-way nesting with horizontal resolutions of 27, 9, and 3 km. The majority of the North Atlantic Ocean and North America is covered by the outermost domain. Both nested domains move to keep the model TC in the center area of the domains. All three domains have 43 vertical levels with the model top at 10 hPa. The integration is conducted for 126 h beginning at 1200 UTC 11 September. The details of the model physics configuration and initialization processes can be found in Munsell et al. (2015, 2017) and Zhang and Weng (2015).

Figure 1 compares the track and intensity of model-derived Edouard to the best-track analysis by the National Hurricane Center (NHC). The PSU WRF real-time forecast predicts the track of the observed storm well on the whole. The comparatively large deviation of the modeled track from the observation mainly occurred before 1800 UTC 13 September, especially at the beginning of the simulation (Fig. 1a). Thereafter, deviations between the observed and modeled track are less than 85 km. The model also predicts very well the nearly rapid intensification after 1200 UTC 14 September, though about 12 h later than observation (Fig. 1b). Both the simulated and observed storms reach their maximum intensity at around 1200 UTC 16 September except that the predicted Edouard is slightly stronger than that estimated by the best-track observation. The proper prediction of the track and intensity implies that the developing process of Edouard may have been well captured by the numerical model, based on which the development of Edouard will be examined in detail. In this work, we focus on the development of Edouard in the isentropic framework proposed by PM13 and subsequently adapted for TC studies by Mrowiec et al. (2016)

and Pauluis and Zhang (2017). According to the time variation of minimum sea level pressure (MSLP; Fig. 1b), the development of Edouard can be partitioned into four consecutive stages: stage I: initial spinup (1200 UTC 11 September–1200 UTC 12 September), stage II: slow intensification (1200 UTC 12 September–1200 UTC 13 September), stage III: fast intensification (1200 UTC 13 September–1200 UTC 14 September), and stage IV: rapid intensification (1200 UTC 14 September–1200 UTC 16 September). We further partition stage III into stages III$_1$ and III$_2$, with 0000 UTC 14 September as the dividing point, subjectively, owing to fluctuation in MSLP over this period.

Following Pauluis (2016), but different from the standard definition as in Emanuel (1994), here the equivalent potential temperature θ_e with respect to ice is defined according to

$$
(C_{pd} + C_i r_T) \ln\left(\frac{\theta_e}{T_f}\right)
$$
$$
= [C_{pd} + r_i C_i + (r_v + r_l)C_l] \ln\left(\frac{T}{T_f}\right) - R_d \ln\left(\frac{p_d}{p_0}\right)
$$
$$
+ (r_v + r_l)\frac{L_{f_0}}{T_f} + r_v\frac{L_v}{T} - r_v R_v \ln(H), \quad (1)
$$

where T is the temperature, H is the relative humidity, and p_d is partial pressure of dry air; C_{pd}, C_i, and C_l are the specific heat capacities at constant pressure of dry air, ice, and liquid water, respectively, while r_v, r_i, r_l, and $r_T = r_v + r_l + r_i$ are the mixing ratios for water vapor, liquid water, ice, and total water, respectively; $p_0 = 10^5$ Pa and $T_f = 273.15$ K are the reference pressure and freezing temperature for water under atmospheric pressure, respectively; R_d and R_v are the specific gas constants of dry air and water vapor; and L_v and L_{f_0} are the latent heat of vaporization taken at the actual temperature and the triple point, respectively.

Figure 2 shows the y–z cross sections of equivalent potential temperature across the center of Edouard from 1200 UTC 12 September to 1200 UTC 16 September with intervals of 12 h. At the end of stage I (Fig. 2a), the equivalent potential temperature is relatively high in the lower troposphere in the vicinity of Edouard's center. Near the maximum low-level θ_e, there is positive perturbation temperature.[1] During stage II (Figs. 2b,c), the low-level θ_e increases gradually and a warm core (denoted by the large perturbation temperature) develops in

---

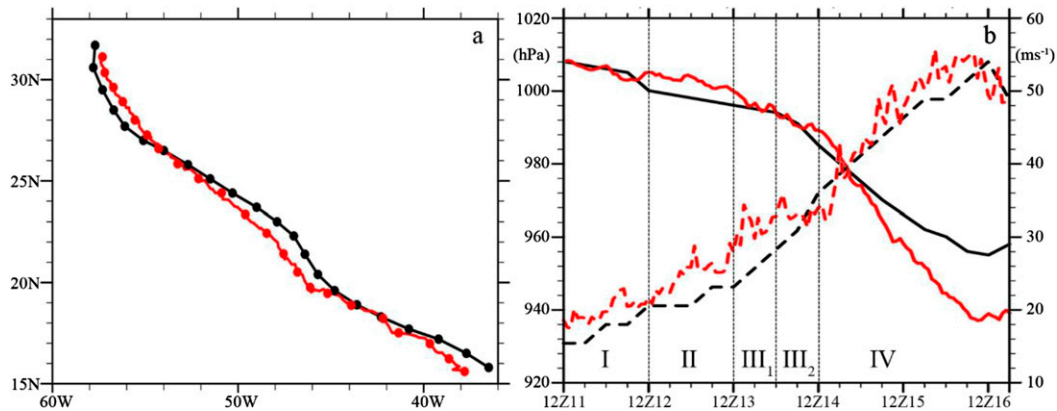[1] The perturbation temperature is derived by removing the domain-averaged temperature from the temperature.

FIG. 1. The NHC best-track analysis (black) and model forecast (red) of (a) track and (b) minimum sea level pressure (solid line) and maximum surface wind (dashed line) of Hurricane Edouard. The thin dashed lines denote the onset of stages II, III$_1$, III$_2$, and IV from left to right, respectively.

the low levels. Meanwhile, the mid- to upper-level θ_e increases on the north side of Edouard's center. At 1200 UTC 13 September (Fig. 2c), the region with $\theta_e > 345$ K in the mid- to upper levels connects with that in the lower troposphere and forms a column of relatively high-θ_e air tilting toward the north from the low to upper levels. Such an apparent tilt is attributed to the remarkable vertical wind shear (~ 11 m s^{-1}; Munsell et al. 2017, their Fig. 6a). In the following 12 h (III$_1$; Fig. 2d), the low- and upper-level θ_e continues to increase while the low- to midlevel positive perturbation temperature penetrates to the upper troposphere. As discussed in Munsell et al. (2017), enhanced convection and vortex precession likely lead to the reduction of the tilt of the air column with high θ_e in stage III$_1$ (Figs. 2c,d). After 0000 UTC 14 September (stage III$_2$), the vertical wind shear begins to decay. Accordingly, the air column with high θ_e and the warm core become upright at 1200 UTC 14 September (Fig. 2e). As a result of the increase of θ_e in the middle troposphere, Edouard's center area is occupied by the air parcels with $\theta_e > 350$ K from the low to upper troposphere. Corresponding to the rapid intensification, the low-level θ_e undergoes a significant increase owing to the enhanced vertical transport of high entropy from the sea surface after 1200 UTC 14 September (Figs. 2f–i). From the low-level high-θ_e region near the storm center, two air plumes with high θ_e extend upward to the upper troposphere, which correspond to the deep eyewall convection as in the wind-induced surface heat exchange (WISHE; Emanuel 1986; Rotunno and Emanuel 1987). At the same time, the upper-level high θ_e exhibits a tendency to expand downward in the eye region. Hence, θ_e is relatively low between $z = 3$ and 9 km in the eye. The superposition of low θ_e and large positive perturbation temperature between $z = 3$ and 9 km in the eye means that the relative humidity is rather low in that region. From Figs. 2g–i,

we can see that θ_e does not increase monotonically from the outer region to center area when the TC is strong and has a well-defined eye.

The relatively low midlevel θ_e in the eye and the vertical alignment of the air column with high θ_e shown in Fig. 2 can be easily identified in Fig. 3. Figure 3 further indicates that the intensification of Edouard is related to an increase of the area occupied by high-θ_e air ($\theta_e > 350$ K). Air parcels with such high θ_e are very rare in the early stages (Figs. 3a,d,g) but form a coherent envelope around the storm center after intensification (Figs. 3c,f,i). Moreover, the eyewall appears as an annulus with $\theta_e > 350$ K while the eye is occupied by the air parcels with a relatively low equivalent potential temperature when Edouard becomes intense.

3. Isentropic analysis of Edouard from formation to intensification

The vertical circulation is important to the atmospheric energy and momentum transfer in TCs. In the literature, TC's vertical circulation is usually discussed via examining the Eulerian-mean circulation, obtained via averaging the velocity at constant height or pressure. By averaging the vertical mass flux in terms of equivalent potential temperature, Mrowiec et al. (2016) obtained a mean vertical circulation of a mature TC on moist isentropes. It is found that the mass transport in the isentropic circulation is much larger than the one represented by the Eulerian-mean secondary circulation. The current study adopts the conditional averaging method used in Mrowiec et al. (2016) in examining the evolution of the dynamic and thermodynamic fields related to Edouard intensification and in depicting a comprehensive description of TC development through the isentropic analysis.
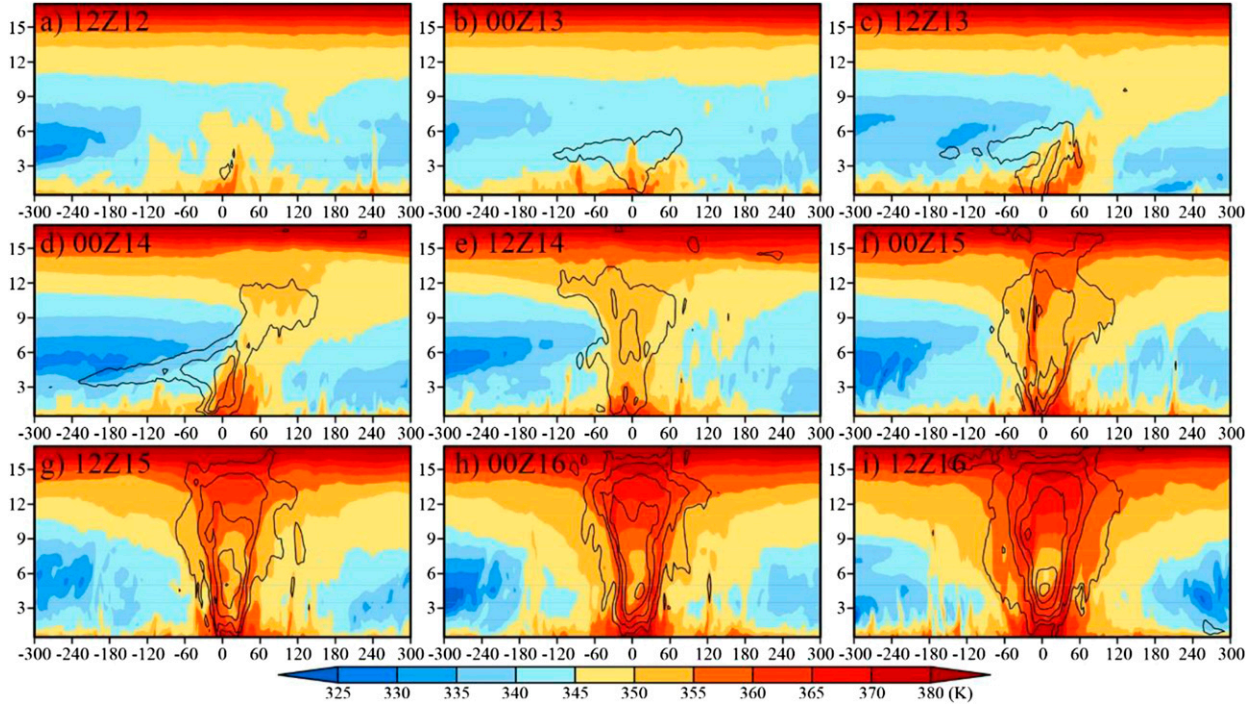
FIG. 2. The evolution of equivalent potential temperature (shading) and perturbation temperature (contours with intervals of 2 K) in the vertical cross section centered at the storm center with north–south orientation over the development of Edouard. The horizontal and vertical axes denote the radius and altitude (km), respectively. The minimum value denoted by the contours is 2 K.

a. Definition of variables for the isentropic analysis

Following Mrowiec et al. (2016), we define an isentropic integral as

$$\langle f \rangle (\theta_{e_0}, z, r_0, t) = \iint_A f(x, y, z, t) \delta \{\theta_{e_0} - \theta_e(x, y, z, t)\}$$

$$\times \delta \{r_0 - r(x, y)\} dx \, dy, \qquad (2)$$

where (θ_{e_0}, z, r_0) denotes the spatial position of an air parcel in the isentropic coordinates, $\delta\{\cdot\}$ is the Dirac delta function, and r and r_0 represent the distances to storm's center. The horizontal integral is taken over the domain A centered at storm's center with side length of 600 km. In this work, the function defined in Eq. (2) is approximated by averaging f over the finite-size θ_e and r bins; that is, $\theta_{e_0} - 0.5 < \theta_e \leq \theta_{e_0} + 0.5$ K and $r_0 - 1.5 < r_0 \leq r_0 + 1.5$ km, respectively.

Replacing f in Eq. (2) with ρw, the isentropic vertical mass flux $\langle \rho w \rangle$ can be written as

$$\langle \rho w \rangle (\theta_{e_0}, z, r_0, t) = \iint_A \rho w(x, y, z, t) \delta \{\theta_{e_0} - \theta_e(x, y, z, t)\}$$

$$\times \delta \{r_0 - r(x, y)\} dx \, dy. \qquad (3)$$

The isentropic mass flux integrated over the whole domain is given by

$$\langle \rho w \rangle_{\theta_e} (\theta_e, z, t) = \int_0^\infty \langle \rho w \rangle (\theta_e, z, r', t) dr'. \qquad (4)$$

According to Mrowiec et al. (2016), the isentropic streamfunction can be obtained by integrating the mass flux defined by Eq. (4); that is,

$$\Psi_{\theta_e} (\theta_e, z, t) = \int_0^{\theta_e} \langle \rho w \rangle_{\theta_e} d\theta'_e. \qquad (5)$$

To ensure that the streamfunction vanishes at large θ_e, the domain-averaged vertical velocity has been removed in the calculation of isentropic streamfunction, as in Mrowiec et al. (2016).

b. Evolution of Edouard's isentropic circulation

Figures 4a–e and 5a–e present the θ_e–z cross sections of mean isentropic streamfunction and vertical mass flux averaged over stages I, II, III$_1$, III$_2$, and IV, respectively. The isentropic vertical circulation of Edouard is for the most part similar to that of an idealized hurricane examined in Mrowiec et al. (2016, their Figs. 4 and 7a). In all developing stages of Edouard (Figs. 4a–e), the
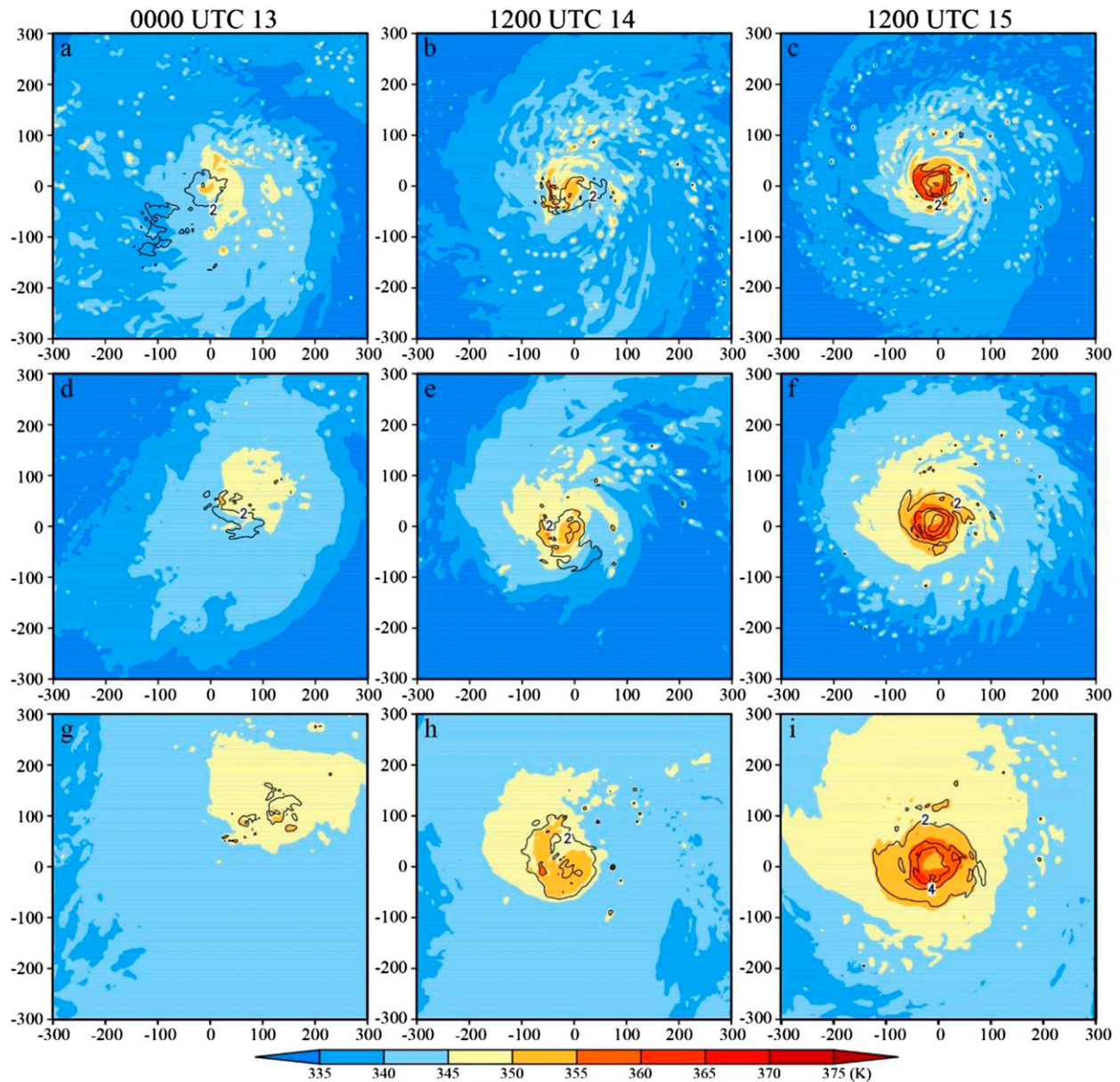
FIG. 3. (a)–(c) Horizontal distribution of equivalent potential temperature (shading) and perturbation temperature (contours) at $t = 36$, 72, and 96 h in the storm-centered area at $z = 3$ km. (d)–(f),(g)–(i) As in (a)–(c), but for $z = 6$ and 9 km, respectively. The area is centered at Edouard's center with side length of 600 km. The minimum value denoted by the contours is 2 K.

isentropic streamfunction is negative, which indicates that the atmospheric overturning corresponds to a combination of ascending air parcels with high θ_e and subsiding air parcels with lower θ_e as confirmed in Figs. 5a–e. Different from the Eulerian framework highlighting the deep convection, the minimum value of isentropic streamfunction is located below 5 km (Figs. 4a–e), which suggests that shallow convection plays a dominant role in the vertical mass transport during the intensification of Edouard. This is consistent

with that found by Mrowiec et al. (2016) in an idealized hurricane and with recent high-resolution simulations and satellite-based studies that identified the occurrence of shallow and moderate precipitation (and convection) as a key indicator that intensification is occurring (e.g., Rogers 2010; Zagrodnik and Jiang 2014; Alvey et al. 2015; Tao and Jiang 2015; Zawislak et al. 2016). Corresponding to the minimum, there are maxima of upward and downward mass fluxes near the surface on the high- and low-θ_e sides, respectively (Figs. 5a–e). The former is
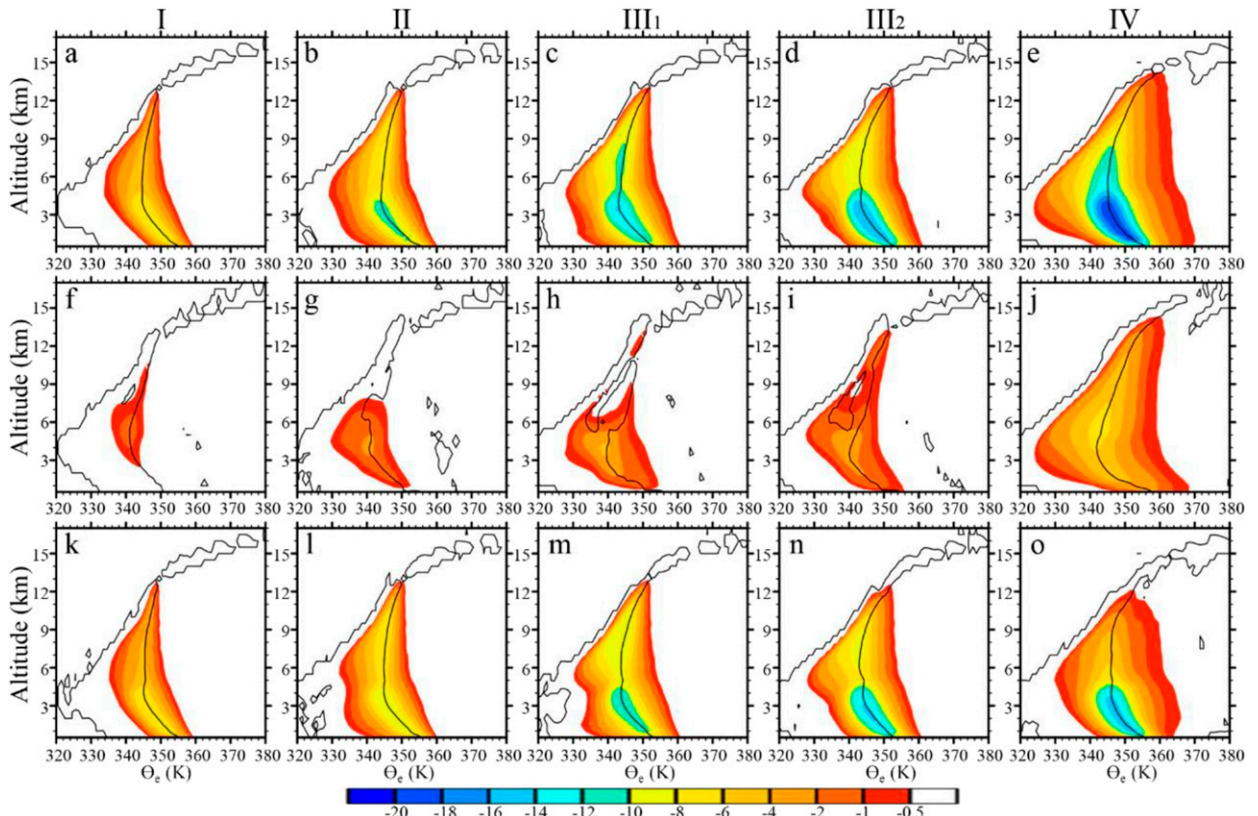
FIG. 4. (a)–(e) θ_e–z cross section of mean isentropic streamfunction ($10^9\,\mathrm{kg\,m^{-2}\,s^{-1}}$) averaged in stages I, II, III$_1$, III$_2$, and IV, respectively. (f)–(j),(k)–(o) As in (a)–(e), but for the streamfunction associated with the axisymmetric and asymmetric components of the flow, respectively. The black contours denote the value of mass flux is zero.

associated with the release of convective available potential energy (CAPE) accumulated via WISHE as well as horizontal transport of higher-moist-entropy air from the outer environment surrounding the storm (Xu and Wang 2010) and, thus, not only contributes to the upward mass transport but also transfers the high-entropy air near the surface upward to fuel the storm intensification. The latter is attributable to strong downdrafts induced by evaporative cooling and large-scale subsidence far away from the storm. These compensating downdrafts can enhance sea surface fluxes of sensible and latent heat and, thus, also favor the accumulation of CAPE.

Although the general pattern of the isentropic circulation is similar in all developing stages of Edouard, considerable variations occur as the storm intensifies. The intensification of Edouard corresponds to a steady decrease in the isentropic streamfunction minimum, an increase in the overall mass transport (both upward and downward), a deepening of the circulation, and a shift of the ascent (descent) toward a higher (lower) value of θ_e (Figs. 4 and 5). From Figs. 5a–e, we can see that both the

near-surface and upper-level upward mass fluxes keep increasing as Edouard intensifies. Near the surface, the upward mass flux expands toward higher θ_e (from 360 to 370 K). In the upper troposphere, strengthening of the upward mass flux is manifested as the rise of the maximum value from stages I to III$_1$ and then as the expansion to higher θ_e in stages III$_2$ and IV.

In stage I (Fig. 5a), the significant downward mass flux mainly occurs in the lower troposphere below the melting level ($z \sim 5\,\mathrm{km}$) and in the upper levels between $z = 9$ and 12 km on the low-θ_e side. From stages II to IV (Figs. 5b–e), the low-level downward mass flux first increases at $z \sim 3\,\mathrm{km}$ and then in lower levels. In the upper troposphere, the downward mass flux strengthens and exhibits an expansion to lower levels toward lower θ_e from stages I to III$_1$ (Figs. 5a–c). In stages III$_2$ and IV (Figs. 5d,e), the downward mass flux weakens in the upper levels, while it enhances in the middle troposphere at low θ_e ($\leq 335\,\mathrm{K}$). The substantial shift of the downward motion toward low values of θ_e is an indication that the storm moves toward dry and colder air masses as shown in Fig. 1a.
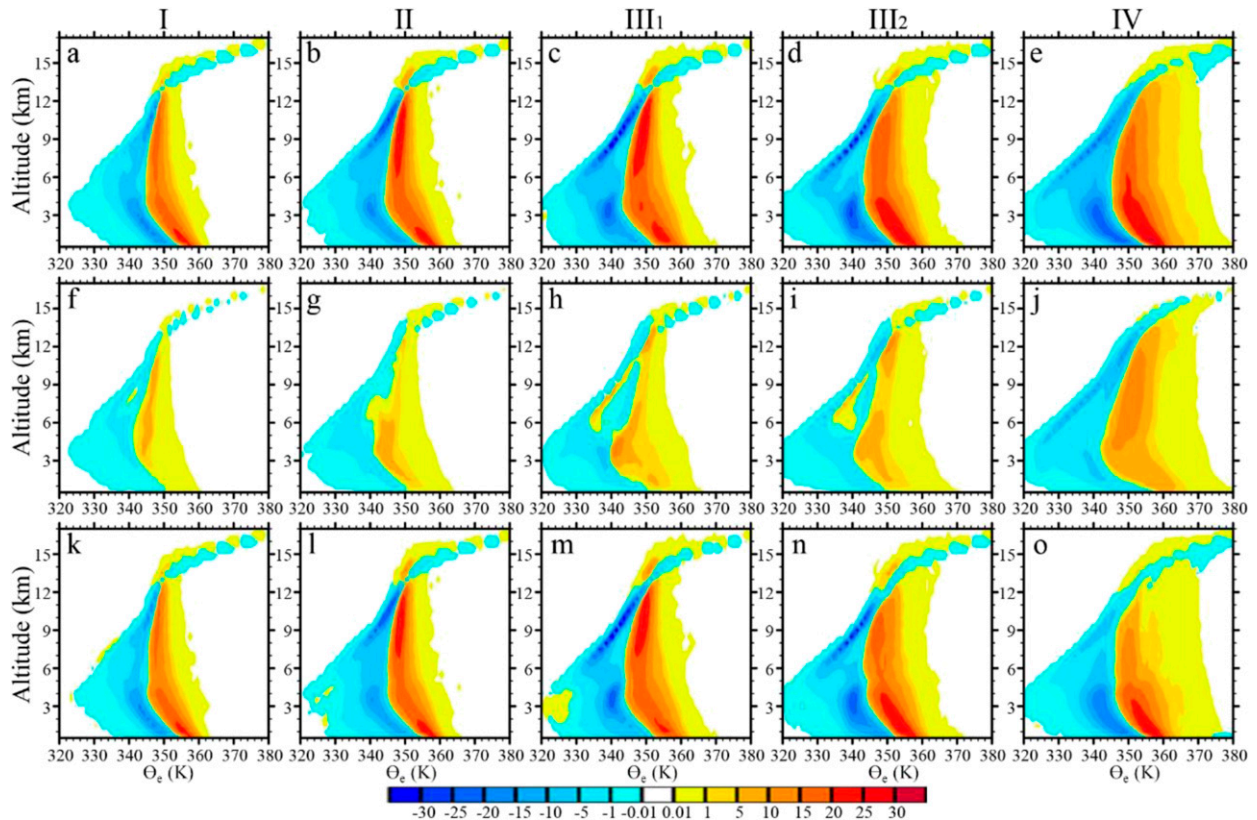
FIG. 5. (a)–(e) θ_e–z cross section of mean isentropic mass fluxes ($10^8\,\mathrm{kg\,m^{-2}\,s^{-1}\,K^{-1}}$) averaged in stages I, II, III$_1$, III$_2$, and IV, respectively. (f)–(j),(k)–(o) As in (a)–(e), but for the mass flux associated with the axisymmetric and asymmetric convection, respectively.

To better assess the changes in the isentropic circulation during the intensification of Edouard, we separate the isentropic mass flux spatially into three distinct categories following Mrowiec et al. (2016): very warm and moist air with $\theta_e > 352\,\mathrm{K}$, corresponding qualitatively to the air rising in the eyewall; warm and moist air with $344 < \theta_e \leq 352\,\mathrm{K}$ rising in deep convective towers, and cold and dry environmental air with $\theta_e \leq 344\,\mathrm{K}$. Figure 6 shows the vertical mass transport and fractional area associated with each airmass category at different stages of Edouard's evolution within the radius of 300 km. In the initial formation stage, the values of $\theta_e > 352\,\mathrm{K}$ are characteristic of the uppermost troposphere and of near-surface air (Fig. 6a), while most of the troposphere is composed of air parcels with $344 < \theta_e \leq 352\,\mathrm{K}$ and $321 < \theta_e \leq 344\,\mathrm{K}$ (Figs. 6f,k). The central part of the storm ($r < 100\,\mathrm{km}$) is more humid and contains more air with intermediate values of θ_e, while the outer region ($r > 100\,\mathrm{km}$) is drier and contains mostly air with low values of θ_e. Through the WISHE, the boundary layer becomes a reservoir of very warm and moist air that can rise through the lower troposphere, but the associated mass flux drops sharply at the top of the boundary layer

likely as a result of strong entrainment (Fig. 6a). From Fig. 6f, we can see that most of the rising motion in stage I is associated with air parcels with intermediate θ_e values between 344 and 352 K that are characteristic of deep convection. The presence of significant upward mass fluxes away from Edouard's center, with $r > 150\,\mathrm{km}$, indicate that deep convection is active in the outer region of Edouard during stage I (Figs. 6a,f).

In stages II and III$_1$, the upward transport of air with $344 < \theta_e \leq 352\,\mathrm{K}$ strengthens significantly at a distance beyond 100 km from the storm center (Figs. 6g,h), responsible for the remarkable strengthening of the isentropic circulation shown in Figs. 4b,c and 5b,c. Although the positive mass flux of very warm and moist air ($\theta_e > 352\,\mathrm{K}$) intensifies near the storm center, it remains a small contributor to the overall mass transport (Figs. 6b,c). Figures 6l and 6m show a noticeable enhancement of subsidence below the melting level ($z \sim 5\,\mathrm{km}$) outside of $r = 100\,\mathrm{km}$, corresponding to convective and mesoscale downdrafts commonly observed in the outer rainbands. The cold and dry air ($\theta_e < 344\,\mathrm{K}$) is on average moving downward, consistent with the downward extension of evident
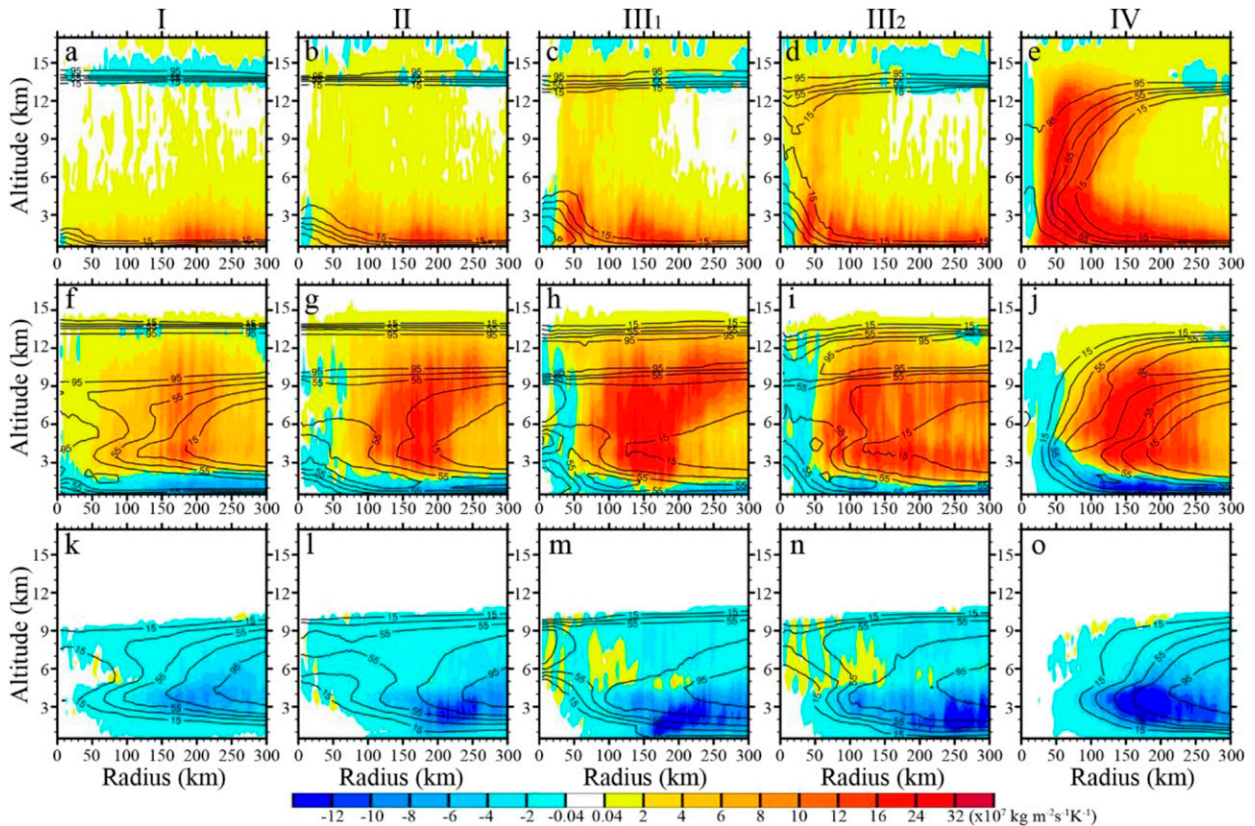
FIG. 6. (a)–(e) Radius–height cross section of mean mass fluxes (shading) and fractional area (contours) associated with an equivalent potential temperature higher than 352 K in stages I, II, III$_1$, III$_2$, and IV, respectively. (f)–(j),(k)–(o) As in (a)–(e), but for the equivalent potential temperature between 344 and 352 K and lower than 344 K, respectively.

downward mass flux in the low troposphere as shown in Figs. 5b and 5c.

The distinct upper-level updraft and low-level downdraft appearing outside of $r = 100$ km shown in Figs. 6g,h and 6l,m indicate that evident stratiform rain processes occur as Edouard intensifies (Mapes and Houze 1995), which may be associated with the remarkable vertical wind shear imposed on Edouard (Houze 1993). Therefore, the significant top-heavy structure of upward mass flux of the air parcels with intermediate values of θ_e ($344 < \theta_e \leq 352$ K) as well as the relatively strong downward mass flux in the lower troposphere on the low-θ_e side in stages II and III$_1$ shown in Figs. 5b and 5c are indicative of stratiform precipitation in the outer rainbands. In addition, Figs. 6b,c and 6g,h show that as Edouard intensifies the outer rainbands shift inward gradually. Meanwhile, a strong upward mass flux develops near the radius of about 50 km, where the azimuthal expansion of the area with very high θ_e (>352 K) is conspicuous in accord with the eyewall development (Figs. 6b,c). Inside of the eyewall, there is noticeable downward mass flux first in the lower troposphere and then extending upward (Figs. 6b,c and 6g,h), which implies that Edouard's eye was first formed in the lower troposphere.

The later developing stages of Edouard (III$_2$ and IV) are characterized by a substantial increase in the upward mass transport of air with very high θ_e (>352 K) (Figs. 5d,e), which is due to the eyewall development (Figs. 6d,e). Inside of the eyewall, the downward mass transport at high θ_e (>352 K) becomes dominant throughout the troposphere (Fig. 6e). Outside the eyewall, the upward mass flux of air parcels with intermediate values of θ_e ($344 < \theta_e \leq 352$ K) associated with stratiform processes in the outer rainbands weakens slightly above $z = 6$ km (Figs. 6i,j), a signature of weakened stratiform precipitation and vertical alignment of the primary vortex. The remarkable downward mass transport persists below the melting level ($z = 5$ km) (Figs. 6i,j and 6n,o), but at stage IV near the surface, the downward mass flux comes predominantly from air with intermediate values of θ_e (Figs. 6j,o).

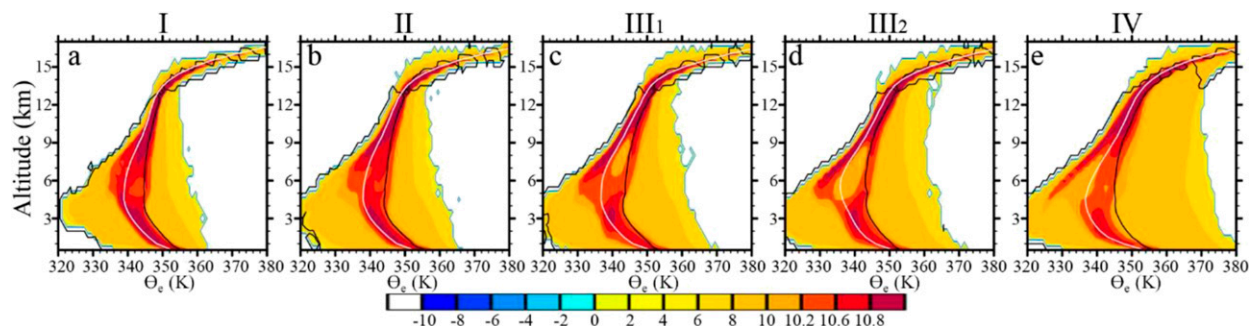To assess the contributions from asymmetric versus axisymmetric vertical transport to Edouard's intensification,

FIG. 7. Natural log of mean area of the air with θ_e between $\theta_e - 0.5$ K and $\theta_e + 0.5$ K in stages (a) I, (b) II, (c) III$_1$, (d) III$_2$, and (e) IV, respectively. The black contours denote the value of mass flux is zero. The white curves represent the mean θ_e averaged over the whole domain.

we further divide the isentropic streamfunction and mass flux into axisymmetric and asymmetric components (Figs. 4f–o and 5f–o). In the early development of Edouard (Figs. 4f and 5f), the axisymmetric convection is rather weak initially while the associated isentropic streamfunction mainly confines in the middle troposphere. As Edouard intensifies (stages II and III), the vertical mass transport induced by axisymmetric convection increases in the lower troposphere and at upper levels (Figs. 5g–i). The corresponding isentropic circulation penetrates both downward and upward while increasing in strength (Figs. 4g–i). By stage III$_2$, the isentropic circulation reaches above $z = 12$ km (Figs. 4i, 5i), which could be a result of the enhanced axisymmetric deep convection following the vertical alignment of the storm as indicated in Figs. 2d and 2e. In the following

rapid-intensification stage (IV; Figs. 4j, 5j), the upward mass flux and streamfunction related to axisymmetric ascent strengthen considerably, especially in the mid- to upper troposphere. The distinct symmetric upward mass flux in the whole troposphere on the high-θ_e side denotes the well-defined eyewall signature as shown in Fig. 6e while the compensating subsidence reaches to much lower θ_e, resulting in a much wider and deeper vertical circulation in θ_e–z coordinates.

For the asymmetric convection, Figs. 4k–o and 5k–o show that the associated isentropic streamfunction and mass transport experience substantial enhancement in the lower troposphere as Edouard intensifies, especially in stages III$_2$ and IV. In the early stages (I, II, and III$_1$; Figs. 4k–m, 5k–m), the upper-level isentropic streamfunction and mass flux strengthen considerably
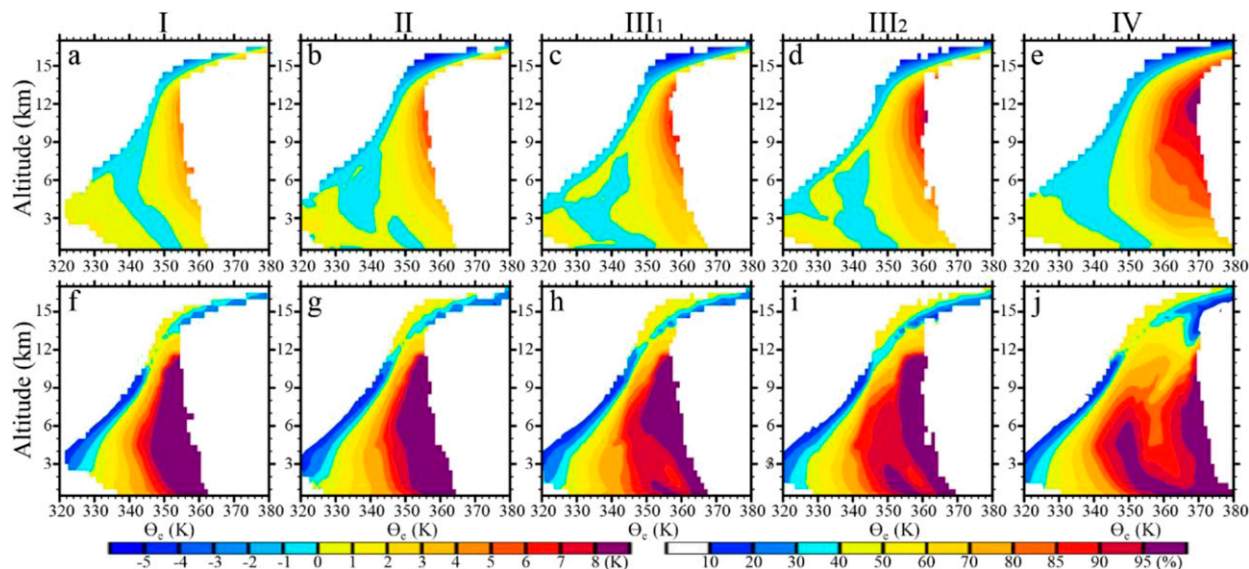

FIG. 8. (a)–(e) θ_e–z cross section of isentropic-mean temperature perturbation (K) averaged in stages I, II, III$_1$, III$_2$, and IV, respectively. (f)–(j) As in (a)–(e), but for the isentropic-mean relative humidity.
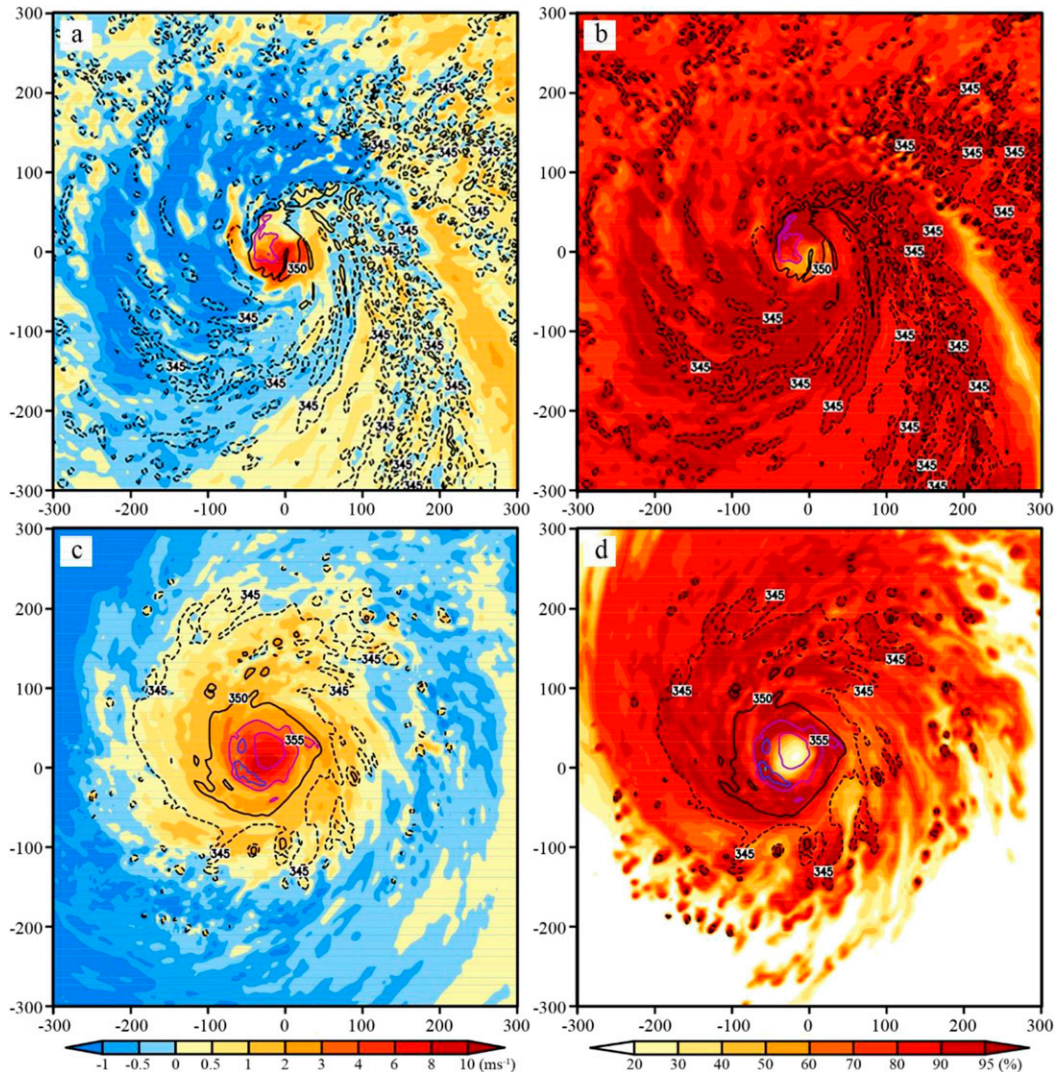
FIG. 9. (a),(b) Plan view of (a) perturbation temperature and (b) relative humidity at $z = 1$ km at 0000 UTC 14 Sep. (c),(d) As in (a) and (b), respectively, but at $z = 7$ km at 1200 UTC 14 Sep.

due to voluminous, asymmetric convection in the outer rainbands induced by the tilting of the storm under the effect of strong vertical wind shear as displayed in Figs. 2a–d. In later stages (III$_2$ and IV) with vortex alignment and rapid intensification, the isentropic streamfunction and mass flux associated with asymmetric convection weakens significantly in the mid- to upper levels (Figs. 4n,o, 5n,o).

Comparing Figs. 4f–j and 5f–j with Figs. 4k–o and 5k–o, we can see that the asymmetric convection makes vital contribution to the isentropic circulation, particularly in the lower troposphere. Even in the most intense stage (IV; Figs. 4o and 5o), the isentropic mass transport and vertical circulation induced by the asymmetric convection is still substantially larger than that of

axisymmetric convection. In the mid- to upper levels, the top-heavy structure of upward mass flux is primarily induced by the asymmetric processes in stages II and III$_1$ (Figs. 5b,c and 5l,m). However, as the vertical wind shear weakens, the contribution of asymmetric processes to the total vertical mass transport reduces noticeably in the mid- to upper troposphere, and as a result, the top-heavy feature of upward mass flux is less significant than before (Figs. 5d,e and 5n,o). From Figs. 4e, 4j, and 4o, we can see that the axisymmetric convection is important to the development of deep isentropic circulation at stage IV. It is worth mentioning that the features of vertical mass transport in the most intense stage (IV) described above are consistent with the findings of Mrowiec et al. (2016). In fact, the
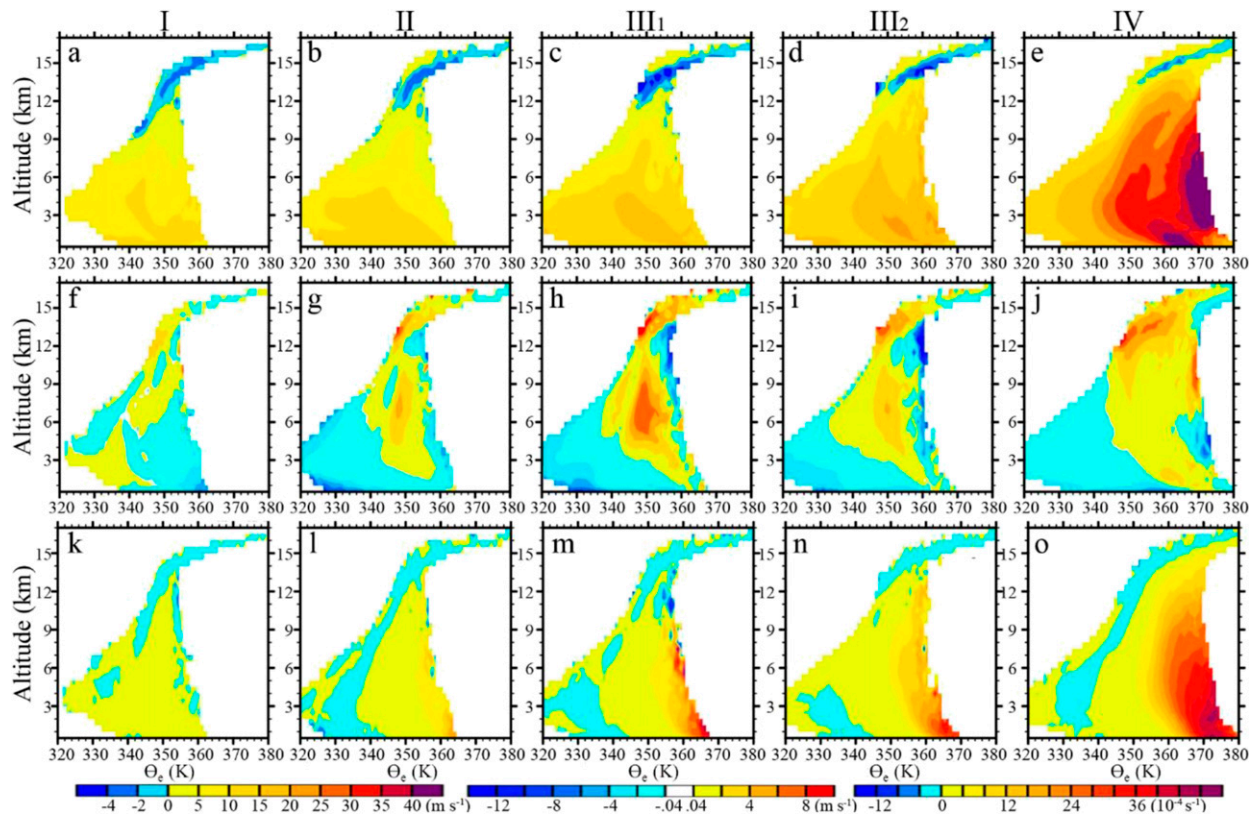
FIG. 10. (a)–(e) θ_e–z cross section of isentropic-mean tangential wind (K) averaged in stages I, II, III$_1$, III$_2$, and IV, respectively. (f)–(j), (k)–(o) As in (a)–(e), but for isentropic-mean radial wind and relative vorticity, respectively.

isentropic streamfunctions in Figs. 4e, 4j, and 4o are similar respectively to Figs. 7a, 8b, and 8a in Mrowiec et al. (2016) except that the center of vertical circulation associated with axisymmetric convection is considerably lower than that displayed in Fig. 8b of Mrowiec et al. (2016).

c. Evolution of Edouard's thermodynamic and dynamic structure in the isentropic framework

The azimuthal areal fraction of each θ_e segment shown in Fig. 6 indicates that distribution of θ_e varies significantly as Edouard intensifies. To examine these variations in greater detail, we compute the area covered by different ranges of θ_e values shown in Fig. 7. Mathematically, this corresponds to the isentropic integral at (θ_e, z) as defined in Eq. (2). In practice, this corresponds to the area by all air parcels at a given level z with an equivalent potential temperature between $\theta_e - 0.5$ K and $\theta_e + 0.5$ K. The initial distribution of the fractional area is typical of the tropical atmosphere (PM13), with the bulk of the air being concentrated near the domain-mean sounding, corresponding to a large reservoir of environmental air (Fig. 7a). The fractional area distribution covers a wide range of θ_e both in the

lower troposphere, primarily indicative of the large variations in the water content, and in the midtroposphere between 6 and 9 km, which can be attributed to the presence of deep, asymmetric mesoscale rainbands. Figure 7a further shows that the rising air parcels cover only a small portion of the domain. In contrast, descending parcels are mostly clustered in very large fractional area, showing that the subsidence occurs primarily within the environment.

As the storm intensifies, the air masses of Edouard are redistributed vertically, which is reflected in the fractional area distribution. In the intensification period (stages II and III; Figs. 7b–d), we can observe three substantial changes. First, there is an increase in amount of air with high θ_e (>352 K), especially near the surface, which coincides with the development of a moist region near the storm center. Second, the midtroposphere between 6 and 9 km exhibits double maxima in fractional area in stage III. The first maximum at low θ_e (≤344 K) corresponds to the descending air in the outer rainbands and the large-scale environment. The second maximum at $\theta_e \sim 344$–348 K is associated with the ascending air in the outer rainbands. The clear separation between the two maxima indicates a lack of horizontal mixing
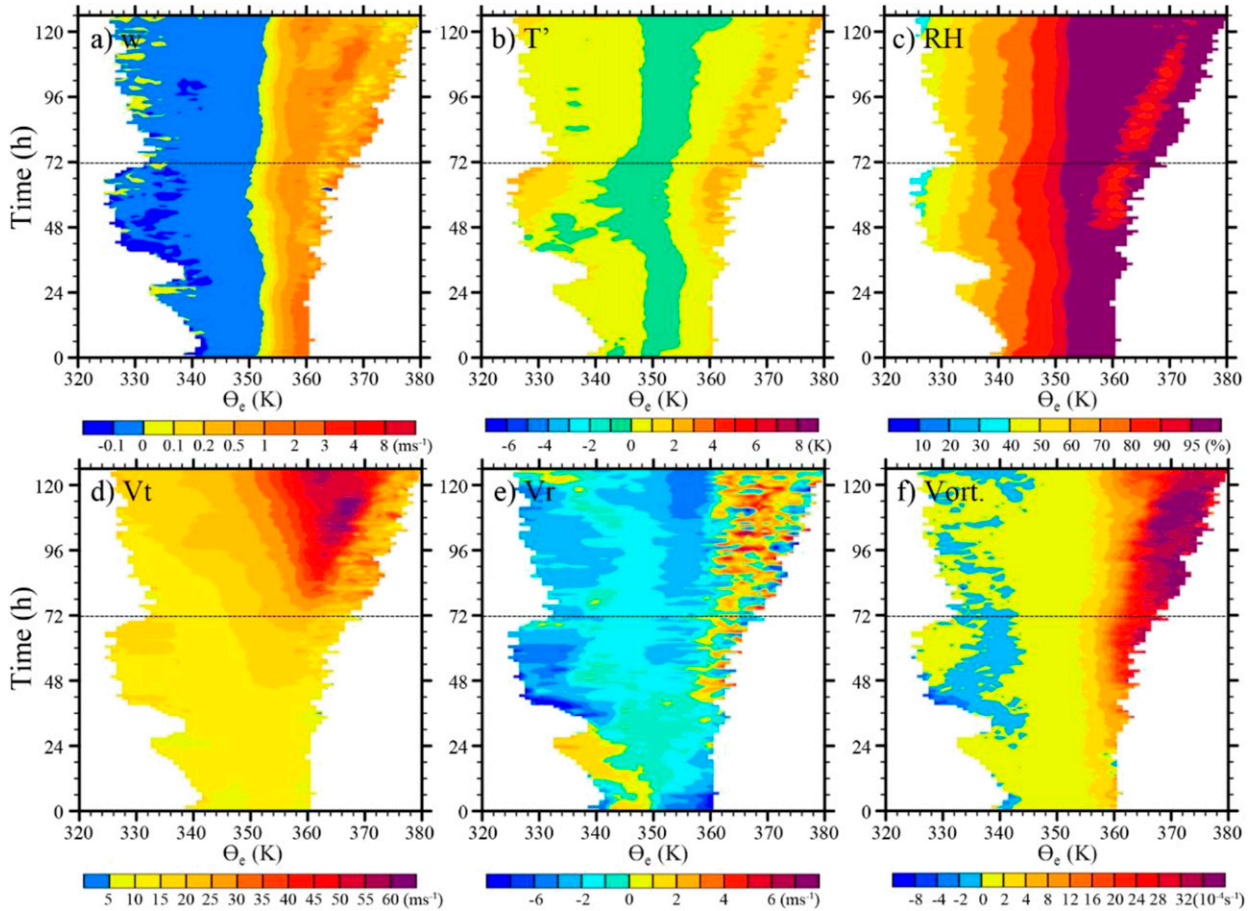
FIG. 11. θ_e–time cross section of isentropic-mean (a) vertical velocity, (b) perturbation temperature, (c) relative humidity (RH), (d) tangential wind, (e) radial wind, and (f) vorticity at $z = 1$ km.

between the outer region and the inner core (Fig. 2). Third, air parcels with $\theta_e < 340$ K appear in the lower troposphere with an equivalent potential temperature lower than the environmental air (denoted by the white curve in Fig. 7) at the same level. These air parcels are the results of convective and mesoscale downdrafts that bring low-θ_e air from above. In addition, melting of frozen precipitation can reduce the equivalent potential temperature of an air parcel, which explains the presence of air parcels with $\theta_e < 330$ K.

The area fraction in the mature stage (IV; Fig. 7e) exhibits similar features, but in a much more pronounced manner. Air parcels with high value of θ_e between 355 and 370 K now present throughout the entire troposphere. The second center of large fractional area has a substantial expansion that includes part of descending air while the first maximum weakens considerably, indicative of the vortex axisymmetrization of Edouard. Finally, there is a substantial intrusion of low-θ_e air below $z = 6$ km, resulting from the convective and mesoscale downdrafts in the outer rainbands. The

emergence of the abovementioned features is directly related to the overturning identified by the streamfunction—a manifestation of the storm intensification corresponding to a midtropospheric buildup of high-θ_e air originating from the surface.

Based on the isentropic density $\langle \rho \rangle$, the mass-weighted mean value of f for all air parcels with a given value of θ_e at level z can be defined as that in PW13:

$$\tilde{f}(\theta_e, z, t) = \frac{\langle \rho f \rangle(\theta_e, z, t)}{\langle \rho \rangle(\theta_e, z, t)}, \tag{6}$$

where we refer to $\tilde{f}$ as the isentropic-mean f. Figure 8 displays the isentropic-mean perturbation temperature and relative humidity during the intensification of Edouard. In θ_e–z space, the substantial perturbation temperature occurs on the high-θ_e side at $z \sim 6.5$ km in the early development stage of Edouard (Fig. 8a), which then shifts upward to the upper levels as the storm intensifies (Figs. 8b–e). With reference back to Figs. 2 and 3,
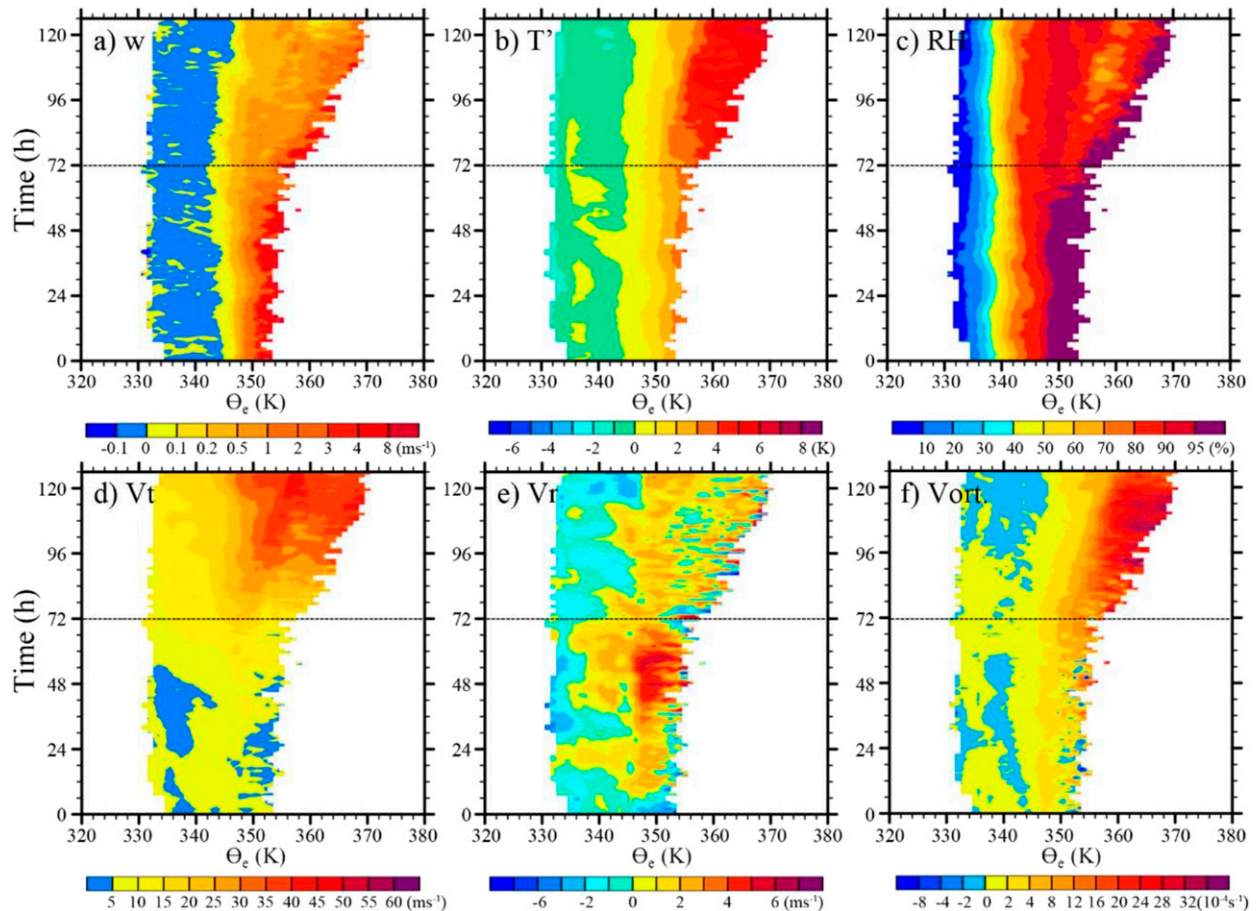
FIG. 12. As in Fig. 9, but at $z = 7$ km.

we can see that the air parcels with high θ_e usually situate in the eye and eyewall. Therefore, the upward shift of the strong perturbation temperature on the high-θ_e side is associated with the development of deep convection in the eyewall and the enhanced detrainment of the air near the tropopause in the eye. The latter can be inferred from the significant decrease in the isentropic-mean relative humidity in the upper troposphere on the high-θ_e side from stages III_2 to IV (Figs. 8i,j), which signifies remarkable intrusion of stratosphere air in the upper levels.

In addition to the significant increase in the mid- to upper troposphere, the isentropic-mean perturbation temperature related to the air parcels with $\theta_e > 350$ K is strengthened in the lower troposphere (Figs. 8a–e). Comparing Figs. 8a–e with Figs. 8f–j, one can find that, on the highest-θ_e side, the increase of low-level perturbation temperature is mainly induced by the eyewall convection, which corresponds to the isentropic-mean relative humidity greater than 95%. However, in the intermediate θ_e between 350 K and the highest θ_e, the increase of perturbation temperature coincides with low

isentropic-mean relative humidity in the lower troposphere. The dry and warm air parcels with intermediate θ_e between 350 K and the highest θ_e in the lower troposphere implies where the eye develops, which is in agreement with the downward mass flux of air parcels with high θ_e in the storm's center area as shown in Figs. 6a–e. Such a feature can also be easily identified in the horizontal distribution of perturbation temperature and relative humidity at $z = 1$ km at 0000 UTC 14 September. Figures 9a and 9b show a comparatively dry and warm patch in the region with $\theta_e > 350$ K, which is the initial signature of a developed eye. Therefore, the two maxima of low-level isentropic relative humidity exhibited in the thermodynamic space θ_e–z displayed in Figs. 8h–j is indicative of the formation of Edouard's eye. From stages II to IV, the increase of perturbation temperature and reduction of relative humidity of air parcels with intermediate θ_e between 350 K and the highest θ_e first appears in the lower troposphere (Figs. 8c,h and Figs. 9a,b), then extends upward to the middle troposphere (Figs. 8d,i and Figs. 9c,d), and finally connects with the dry tongue originating from $z = 15$ km
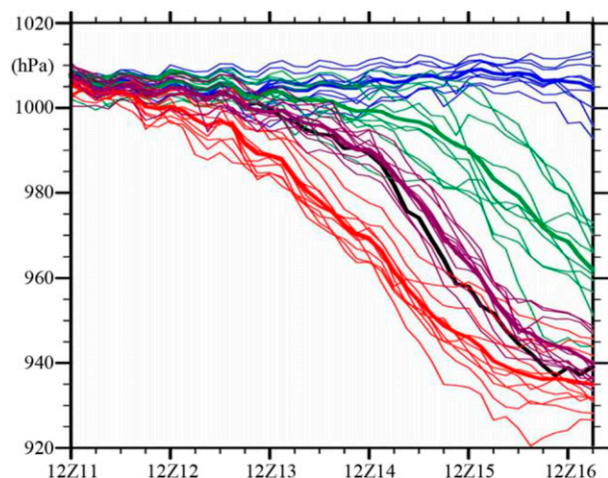
FIG. 13. The 126-h deterministic and ensemble forecasts of minimum sea level pressure of Edouard from 1200 UTC 11 Sep 2014. The thick black curve denotes the deterministic forecast. The thin curves denote the ensemble forecasts in GOOD (purple), GOOD_EARLY (red), GOOD_LATE (green), and POOR (blue) groups. The composite means of the groups are denoted by the thick curves in purple, red, green, and blue, respectively.

on the highest-θ_e side in the rapid-intensification stage (IV; Figs. 8e,j).

Similar to the isentropic-mean relative humidity, the tangential velocity also exhibits two maxima on the high-θ_e side after stage II (Figs. 10a–e). The air parcels with θ_e between 350 and 360 K are partially situated in the eye of Edouard (Figs. 2f–i, 3c,f,i, and 9) and have thus weaker tangential velocity than the air in the eyewall and the region immediately outside of the eyewall. In contrast, the air parcels with $\theta_e > 360$ K are solely found in the eyewall and corresponding to the strongest tangential wind on the highest-θ_e side in the θ_e–z space. During the intensification of Edouard, the prominent variation of radial wind in the θ_e–z space is the enhancement and weakening of the mid- to upper-level radial outflow right outside of the eyewall in the early stages (I, II, and III$_1$; Figs. 10f–h) and later stages (III$_2$ and IV; Figs. 10i,j) of Edouard intensification. This radial outflow maximizes right below the maximum upward mass flux in the upper troposphere and varies coincidently with the maximum upward mass flux in the thermodynamic space θ_e–z (Figs. 10f–j and 5a–e), indicating that it may be associated with the asymmetric convection in the outer rainbands. Figures 10f–j also indicate that the radial outflow above $z = 12$ km strengthens noticeably on the low-θ_e–z side as Edouard intensifies, corresponding to the outflow from the eyewall. In the low levels, the inflow layer outside of the eyewall becomes shallow as Edouard intensifies. In the most intense stage of Edouard, the

inflow outside of the eyewall strengthens notably and radial outflow originated from the eye develops near the surface (Figs. 10j). Different from the above-mentioned variables, the vorticity achieves its maximum on the high-θ_e side (Figs. 10k–o). From stages I to III$_1$, the vorticity of air parcels with high θ_e increases persistently and substantially below $z \sim 9$ km. In stage III$_2$ (Fig. 10n), the large values of positive vorticity extend to the layer above $z = 9$ km on the high-θ_e side. According to Schubert and Hack (1982), this increases the efficiency of heating sources relative to vortex intensification response favorable for storm intensification.

To further examine the evolution of Edouard's structure during its intensification, the time evolution of isentropic-mean variables in the lower and mid- to upper troposphere are presented in Figs. 11 and 12, respectively. Figure 11 shows that, in the low level, the highest θ_e stays at ~360 K in the first 30 h of integration. Similarly, none of the low-level vertical velocity, temperature, and relative humidity fields present noticeable variations on the high-θ_e side before $t = 30$ h. From $t \sim 42$ h, relatively weak ascent, high temperature, and low relative humidity emerge on the high-θ_e side in the lower troposphere (Figs. 11a–c). This corresponds to the development of the eye, as discussed in the previous section. At the same time, the maximum tangential velocity and related radial inflow of the air parcels with θ_e between 350 and 360 K as well as the vorticity on the highest-θ_e side increase significantly (Figs. 11d–f). However, the maximum value of θ_e of air parcels does not increase persistently and substantially until after $t \sim 60$ h. Similar to that occurring in the lower troposphere, the remarkable variations of isentropic-mean variables precede the shift toward higher value of maximum θ_e in the mid- to upper levels. Figure 12 shows that, at $z = 7$ km, the shift toward higher values of maximum θ_e starts at ~72 h with the rapid-intensification onset while the vertical velocity, relative humidity, and radial outflow begin to decrease and the vorticity starts to increase as early as $t = 60$ h in the high-θ_e side.

Figures 11 and 12 indicate that Edouard intensifies in a bottom-up manner in the thermodynamic space θ_e–z. The developing storm experiences a substantial decrease of isentropic-mean vertical velocity, relative humidity, and radial outflow as well as an evident increase of vorticity in the mid- to upper troposphere about 12 h before the start of the near-rapid intensification of Edouard. The remarkable changes of these thermodynamic and dynamics variables may on the other hand be used as a precursor of potential rapid intensification. The abovementioned indicators in the thermodynamic space θ_e–z may have the advantage in that these
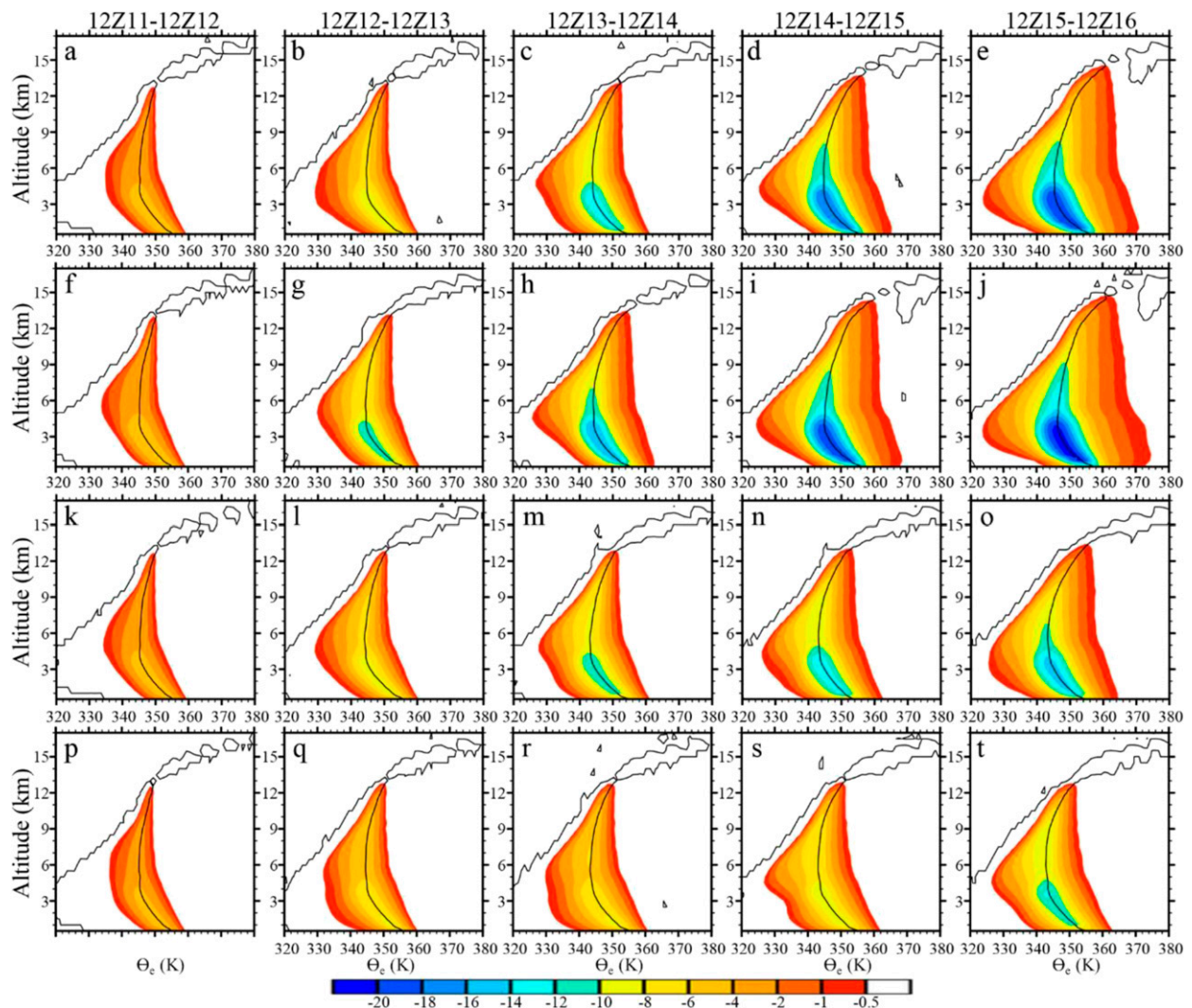
FIG. 14. (a)–(e) θ_e–z cross section of composite 24-h-mean isentropic streamfunction (10^9 kg m^{-2} s^{-1}) derived from the GOOD group. (f)–(j),(k)–(o),(p)–(t) As in (a)–(e), but for GOOD_EARLY, GOOD_LATE, and POOR groups, respectively. The black contours denote the value of mass flux is zero.

indicators combine the usual variables with high θ_e and some of them reflect the changes of TC structure in the inner-core region in θ_e–z space without a prior specification of the location of a storm center.

d. Composite analysis on the intensification of Edouard in the isentropic framework

The results presented in sections 3b and 3c are based on a single deterministic simulation (prediction) of Edouard. To evaluate the robustness of the previous results, a comprehensive composite analysis on the intensification of Edouard derived from the 60-member ensemble simulation is performed in this subsection. This is the same real-time ensemble that was studied in Munsell et al. (2017). The details of the ensemble

configurations can be found in Munsell et al. (2015, 2017) and Zhang and Weng (2015). Following Munsell et al. (2017), four groups of 10 members each are created according to each member's respective rapid-intensification onset time: that is, GOOD, GOOD_EARLY, GOOD_LATE, and POOR (Fig. 13). The GOOD group is composed of 10 members with rapid-intensification onsets at approximately 72 h, which is very close to the deterministic simulation showing in Fig. 1b. The GOOD_EARLY and GOOD_LATE groups are similar to the GOOD group except that rapid intensification starts at 48 and 96 h, that is, 24 h ahead of and lagging that derived from the deterministic simulation, respectively. Ten members without rapid intensification during the simulation period are chosen to create the POOR group.
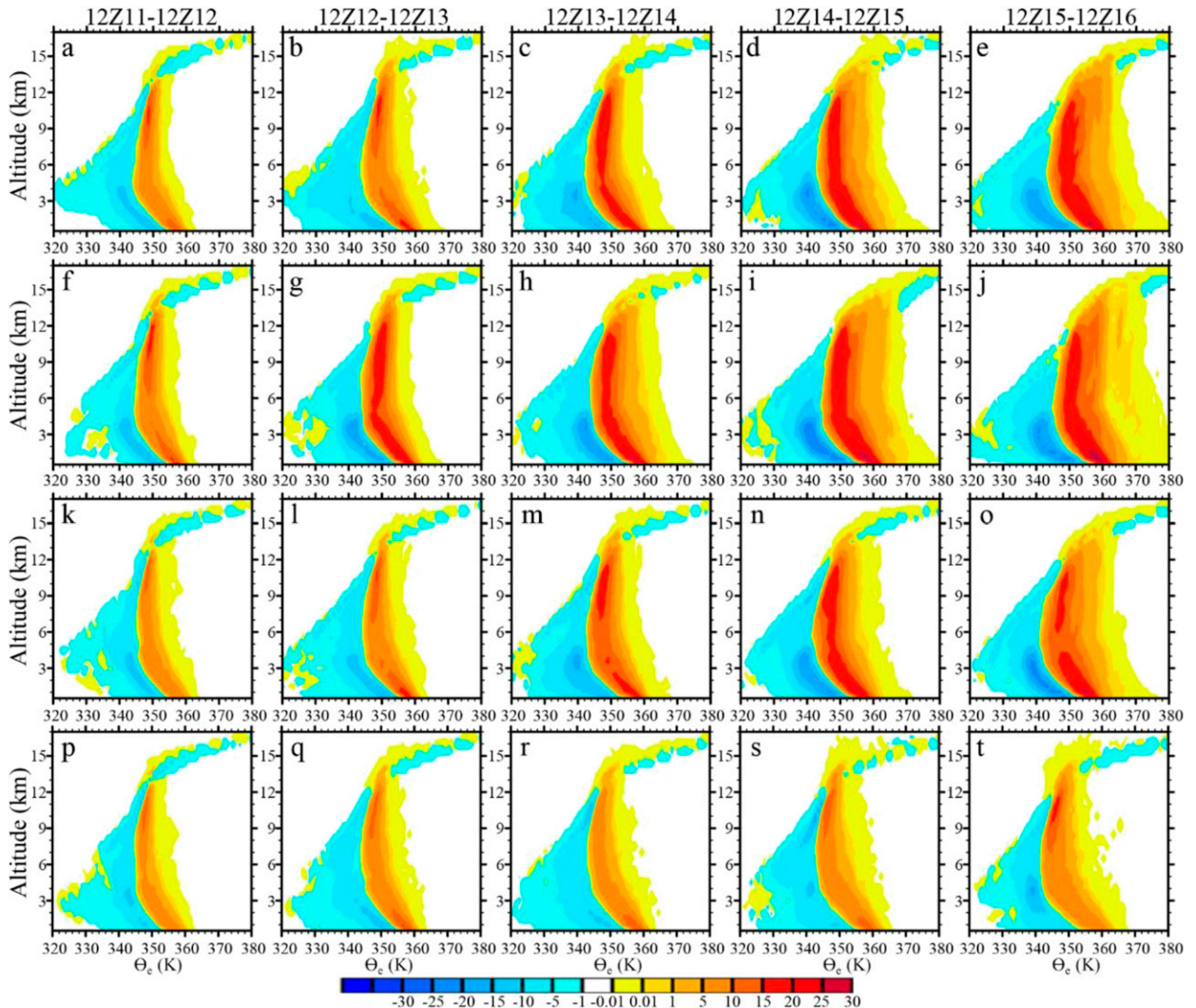
FIG. 15. (a)–(e) θ_e–z cross section of 24-h-mean isentropic mass fluxes (10^8 kg m^{-2} s^{-1} K^{-1}) derived from the GOOD group. (f)–(j), (k)–(o),(p)–(t) As in (a)–(e), but for GOOD_EARLY, GOOD_LATE, and POOR groups, respectively.

Figures 14 and 15 present the 24-h-mean isentropic streamfunction and mass flux of simulated Edouard in the four composite groups. From Figs. 14a–o and 15a–o, we can see that the variations of the isentropic streamfunction and mass flux during the intensification of Edouard in the three GOOD composite groups are quite similar to those in the deterministic simulation except for the differences in magnitudes, which indicates that the intensifying TCs share the similar evolution in the isentropic framework; that is, the streamfunction decreases significantly in both the lower and the upper troposphere, corresponding to the remarkable strengthening of upward mass flux in the troposphere. Before the onset of rapid intensification, the maximum upward mass flux at each level is larger than 2×10^9 kg m^{-2} s^{-1} K^{-1} in the three GOOD composite groups (Figs. 15c,g,n). On the

contrary, in the POOR group, the upward mass flux in the low to midtroposphere is much smaller than this value and the decrease of streamfunction is rather weak during the simulation. Figures 14a–o and 15a–o further indicate that the stronger the vertical mass transport is, the earlier the onset of rapid intensification. The composite analysis on the asymmetric and axisymmetric circulations in the three GOOD composite groups also support the results achieved from the deterministic simulation (figures not shown). Similar to those obtained from the deterministic simulation, the perturbation temperature, tangential velocity, and relative vorticity undergo increases while the relative humidity and radial outflow both experience decreases on the high-θ_e side in the mid- to upper troposphere before the onset of rapid intensification in the three GOOD composite groups
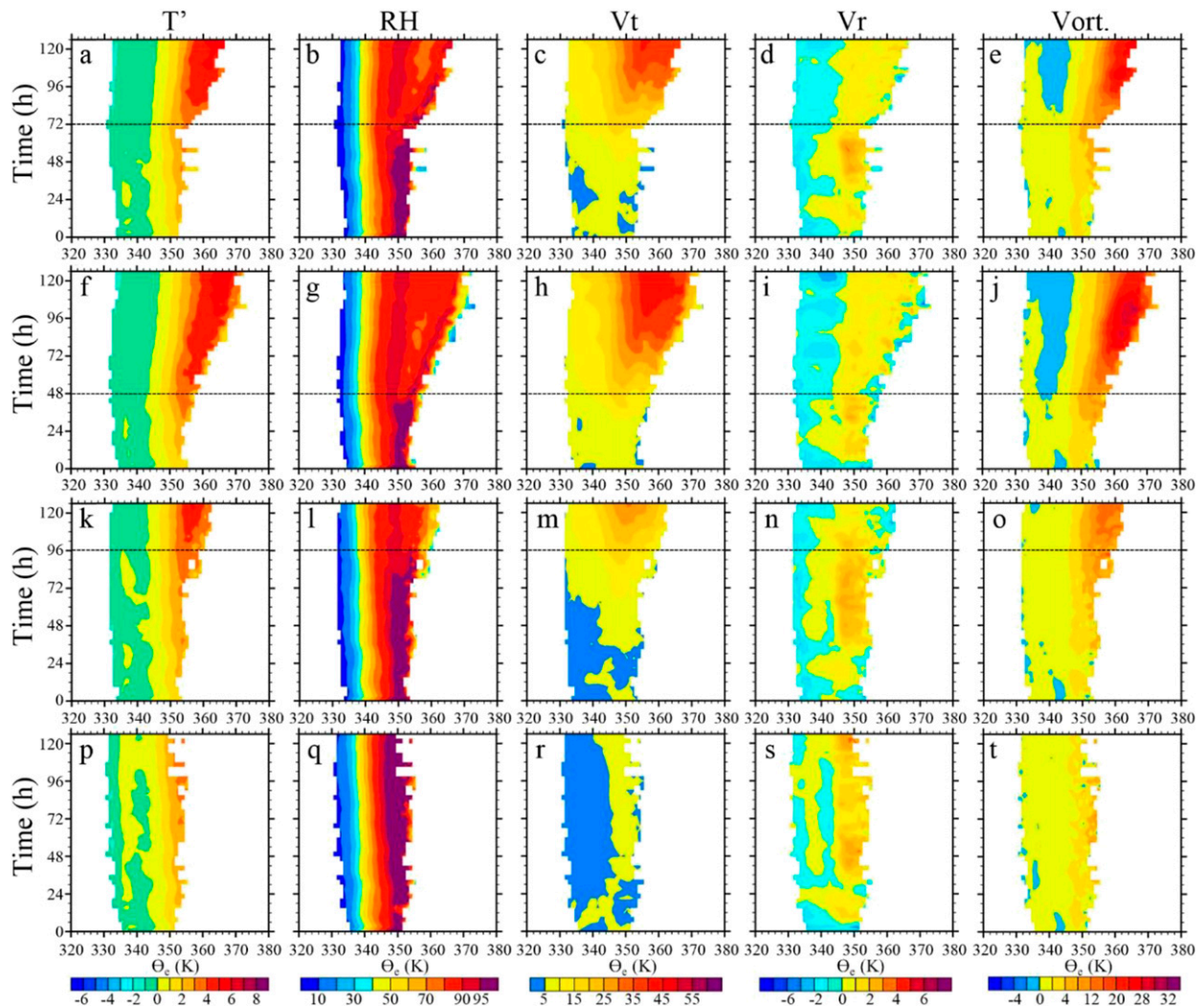
FIG. 16. (a)–(e) θ_e–time cross section of isentropic-mean (a) perturbation temperature, (b) relative humidity (RH), (c) tangential wind, (d) radial wind, and (e) relative vorticity at $z = 7$ km for GOOD group. (f)–(j),(k)–(o),(p)–(t) As in (a)–(e), but for the GOOD_EARLY, GOOD_LATE, and POOR groups, respectively. The dashed lines in (a)–(o) denote the onset of rapid intensification.

(Figs. 16a–o). However, these properties do not satisfy simultaneously in the composite POOR group (Figs. 16p–t). Figure 16 further confirms that the comprehensive account of the time evolution of mid- to upper-level isentropic-mean variables may lead to the evaluation on whether the rapid-intensification process will occur soon in an intensifying TC.

4. Concluding remarks

The isentropic analysis techniques based on sorting the flow properties in the terms of equivalent potential temperature were developed by PM13. In this study, the techniques are used to examine the development of a real-data-simulated hurricane—Edouard (2014)—with the deterministic and 60-member ensemble simulations.

The pattern of the isentropic vertical circulation during the development of Edouard is similar to that obtained by Mrowiec et al. (2016) on the whole, though it is derived from the mature ideal hurricane. The isentropic vertical circulation results from the combination of ascending air parcels with high θ_e and subsiding air parcels with lower θ_e. As Edouard intensifies, the vertical circulation becomes wide via the expansion of upward (downward) mass flux to higher (lower) θ_e. In the early developing stages, the asymmetric convection dominates the variation of vertical circulation. The vertical circulation associated with axisymmetric convection is comparatively weak and starts as a midtropospheric ascent that first spread to the surface before deepening and the development of an eyewall signature after the nearly rapid intensification. As Edouard becomes very

intense, the upper-level upward mass flux induced by asymmetric convection weakens in the outer-core region while the axisymmetric convection turns out to be important to the vertical mass transport in the upper troposphere. However, the asymmetric convection still dominates the vertical mass transport in the low levels.

During the development of Edouard, the total upward mass flux has two maximum centers, situated in the upper and lower troposphere, respectively, in the thermodynamic space θ_e–z. The upper-level center is mainly induced by the updrafts outside of the eyewall while the low-level one basically corresponds to the massive shallow convection in the area with high equivalent potential temperature. In the early developing stages, the upper-level mass flux enhances fast in the maximum center while the increase of upward mass flux is rather trivial below the center. Such a phenomenon is primarily induced by the asymmetric processes. It is suggested that the remarkable vertical wind shear induced distinct stratiform precipitation in the outer-core region, which contributes to the enhancement of upper-level upward mass flux and low- to midlevel downward mass flux. As the vertical wind shear decreases, the stratiform precipitation weakened and the upward mass flux center in the upper levels becomes less evident as before. In the lower troposphere, the upward mass flux in the maximum center experiences persistent enhancement during the intensification of Edouard under the combined effect of axisymmetric and asymmetric processes.

In addition to manifesting that the vertical mass flux and streamfunction in the thermodynamic space θ_e–z in a real-data-simulated TC are quite similar to that derived from an idealized TC as discussed in Mrowiec et al. (2016), the present study further reveals the structural evolution of Edouard via analyzing the isentropic-mean properties during the intensification of Edouard. It is found that the development of the warm core in the eye leads to double maxima along the θ_e axis for both the isentropic-mean relative humidity and tangential velocity. Before the onset of rapid intensification, the isentropic-mean properties such as the mid- to upper-level relative humidity, vertical velocity, and radial outflow decreased considerably while the mid- to upper-level vorticity experiences a distinct increase on the high-θ_e side, suggesting that these properties could be used as indicators for the onset of rapid intensification. Moreover, the isentropic analysis performed here also indicates that as Edouard intensifies the eye characterized by warm and dry core first forms in the low to middle troposphere and then expands upward gradually. Different from the traditional analysis, the abovementioned properties in the thermodynamic space θ_e–z may have the advantages of binning common variables with θ_e that could reflect the changes of TC structure in the inner-core region θ_e–z without a prior specification of the location of a storm center. Therefore, the isentropic framework can be a useful tool in understanding and prediction of TC intensification.

It is worth of mentioning that the formation of the eye during the intensification of Edouard means that the descending air parcels in the eye can reduce the upward mass flux on the high-θ_e side. However, the eye region is usually too small to modify the isentropic vertical circulation considerably. The vertical circulation derived without the contribution of the air parcels within the radius of 30 km is nearly the same as that derived from the whole domain and, thus, the associated isentropic streamfunction can be used to represent the mean trajectories of air parcels outside the eye in the thermodynamic space θ_e–z, as suggested by Mrowiec et al. (2016). In addition, the analysis on the evolution of isentropic streamfunction and vertical mass flux during the intensification of Edouard indicates that the vertical wind shear can affect the isentropic circulation of Edouard substantially. Considering that the isolines of the isentropic streamfunction correspond to the mean trajectories in the θ_e–z space and the thermodynamic cycles of turbulent atmospheric flows can be analyzed through tracing air parcels along the isentropic streamfunction (Pauluis 2016; Pauluis and Zhang 2017), the effect of vertical wind shear on Edouard intensification may be further revealed quantitatively by examining the energetics associated with the thermodynamic cycles of Edouard. This is currently being explored and will be presented in a separate work in the future.

REFERENCES

Alvey, G. R., III, J. Zawislak, and E. Zipser, 2015: Precipitation properties observed during tropical cyclone intensity change. *Mon. Wea. Rev.*, **143**, 4476–4492, doi:10.1175/MWR-D-15-0065.1.

Anthes, R. A., 1971: A numerical model of the slowly varying tropical cyclone in isentropic coordinates. *Mon. Wea. Rev.*, **99**, 617–635, doi:10.1175/1520-0493(1971)099<0617:ANMOTS>2.3.CO;2.

Emanuel, K. A., 1986: An air-sea interaction theory for tropical cyclones. Part I: Steady-state maintenance. *J. Atmos. Sci.*, **43**, 585–604, doi:10.1175/1520-0469(1986)043<0585:AASITF>2.0.CO;2.

——, 1994: *Atmospheric Convection.* Oxford University Press, 580 pp.

——, 1997: Some aspects of hurricane inner-core dynamics and energetics. *J. Atmos. Sci.*, **54**, 1014–1026, doi:10.1175/1520-0469(1997)054<1014:SAOHIC>2.0.CO;2.

Fang, J., and F. Zhang, 2010: Initial development and genesis of Hurricane Dolly (2008). *J. Atmos. Sci.*, **67**, 655–672, doi:10.1175/2009JAS3115.1.

——, and ——, 2011: Evolution of multiscale vortices in the development of Hurricane Dolly (2008). *J. Atmos. Sci.*, **68**, 103–122, doi:10.1175/2010JAS3522.1.

——, and ——, 2012: Effect of beta shear on simulated tropical cyclones. *Mon. Wea. Rev.*, **140**, 3327–3346, doi:10.1175/MWR-D-10-05021.1.

Frank, W. M., 1977: The structure and energetics of the tropical cyclone I. Storm structure. *Mon. Wea. Rev.*, **105**, 1119–1135, doi:10.1175/1520-0493(1977)105<1119:TSAEOT>2.0.CO;2.

Gu, J.-F., Z.-M. Tan, and X. Qiu, 2015: Effects of vertical wind shear on inner-core thermodynamics of an idealized simulated tropical cyclone. *J. Atmos. Sci.*, **72**, 511–530, doi:10.1175/JAS-D-14-0050.1.

Houze, R., Jr., 1993: *Cloud Dynamics.* Academic Press, 573 pp.

——, S. S. Chen, B. F. Smull, W.-C. Lee, and M. M. Bell, 2007: Hurricane intensity and eyewall replacement. *Science*, **315**, 1235–1239, doi:10.1126/science.1135650.

Kieu, C., V. Tallapragada, D.-L. Zhang, and Z. Moon, 2016: On the development of double warm-core structures in intense tropical cyclones. *J. Atmos. Sci.*, **73**, 4487–4506, doi:10.1175/JAS-D-16-0015.1.

Kjellsson, J., K. Döös, F. B. Laliberté, and J. D. Zika, 2014: The atmospheric general circulation in thermodynamical coordinates. *J. Atmos. Sci.*, **71**, 916–928, doi:10.1175/JAS-D-13-0173.1.

Laliberté, F., J. Zika, L. Mudryk, P. Kushner, J. Kjellsson, and K. Döös, 2015: Constrained work output of the moist atmospheric heat engine in a warming climate. *Science*, **347**, 540–543, doi:10.1126/science.1257103.

Mapes, B. E., and R. A. Houze Jr., 1995: Diabatic divergence profiles in western Pacific mesoscale convective systems. *J. Atmos. Sci.*, **52**, 1807–1828, doi:10.1175/1520-0469(1995)052<1807:DDPIWP>2.0.CO;2.

Merrill, R. T., and C. S. Velden, 1996: A three-dimensional analysis of the outflow layer of Supertyphoon Flo (1990). *Mon. Wea. Rev.*, **124**, 47–63, doi:10.1175/1520-0493(1996)124<0047:ATDAOT>2.0.CO;2.

Molinari, J., S. Skubis, and D. Vollaro, 1995: External influences on hurricane intensity. Part III: Potential vorticity structure. *J. Atmos. Sci.*, **52**, 3593–3606, doi:10.1175/1520-0469(1995)052<3593:EIOHIP>2.0.CO;2.

——, D. Knight, M. Dickinson, D. Vollaro, and S. Skubis, 1997: Potential vorticity, easterly waves, and eastern Pacific tropical cyclogenesis. *Mon. Wea. Rev.*, **125**, 2699–2708, doi:10.1175/1520-0493(1997)125<2699:PVEWAE>2.0.CO;2.

Mrowiec, A. A., O. M. Pauluis, and F. Zhang, 2016: Isentropic analysis of a simulated hurricane. *J. Atmos. Sci.*, **73**, 1857–1870, doi:10.1175/JAS-D-15-0063.1.

Munsell, E. B., J. A. Sippel, S. A. Braun, Y. Weng, and F. Zhang, 2015: Dynamics and predictability of Hurricane Nadine (2012) evaluated through convection-permitting ensemble analysis and forecasts. *Mon. Wea. Rev.*, **143**, 4514–4532, doi:10.1175/MWR-D-14-00358.1.

——, F. Zhang, J. A. Sippel, S. A. Braun, and Y. Weng, 2017: Dynamics and predictability of the intensification of Hurricane Edouard (2014). *J. Atmos. Sci.*, **74**, 573–595, doi:10.1175/JAS-D-16-0018.1.

Pauluis, O. M., 2016: The mean air flow as Lagrangian dynamics approximation and its application to moist convection. *J. Atmos. Sci.*, **73**, 4407–4425, doi:10.1175/JAS-D-15-0284.1.

——, and A. A. Mrowiec, 2013: Isentropic analysis of convective motions. *J. Atmos. Sci.*, **70**, 3673–3688, doi:10.1175/JAS-D-12-0205.1.

——, and F. Zhang, 2017: Reconstruction of the thermodynamic cycles in a high-resolution simulation of a hurricane. *J. Atmos. Sci.*, **74**, 3367–3381, doi:10.1175/JAS-D-16-0353.1.

——, A. Czaja, and R. Korty, 2008: The global atmospheric circulation on moist isentropes. *Science*, **321**, 1075–1078, doi:10.1126/science.1159649.

——, ——, and ——, 2010: The global atmospheric circulation in moist isentropic coordinates. *J. Climate*, **23**, 3077–3093, doi:10.1175/2009JCLI2789.1.

Qiu, X., and Z.-M. Tan, 2013: The roles of asymmetric inflow forcing induced by outer rainbands in tropical cyclone secondary eyewall formation. *J. Atmos. Sci.*, **70**, 953–974, doi:10.1175/JAS-D-12-084.1.

——, ——, and Q. Xiao, 2010: The roles of vortex Rossby waves in hurricane secondary eyewall formation. *Mon. Wea. Rev.*, **138**, 2092–2109, doi:10.1175/2010MWR3161.1.

Riemer, M., and F. Laliberté, 2015: Secondary circulation of tropical cyclones in vertical wind shear: Lagrangian diagnostic and pathways of environmental interaction. *J. Atmos. Sci.*, **72**, 3517–3536, doi:10.1175/JAS-D-14-0350.1.

Rivoire, L., T. Birner, and J. A. Knaff, 2016: Evolution of the upper-level thermal structure in tropical cyclones. *Geophys. Res. Lett.*, **43**, 10 530–10 537, doi:10.1002/2016GL070622.

Rogers, R., 2010: Convective-scale structure and evolution during a high-resolution simulation of tropical cyclone rapid intensification. *J. Atmos. Sci.*, **67**, 44–70, doi:10.1175/2009JAS3122.1.

Rossby, C.-G., 1937: Isentropic analysis. *Bull. Amer. Meteor. Soc.*, **18**, 201–209.

Rotunno, R., and K. A. Emanuel, 1987: An air–sea interaction theory for tropical cyclones. Part II: Evolutionary study using a nonhydrostatic axisymmetric numerical model. *J. Atmos. Sci.*, **44**, 542–561, doi:10.1175/1520-0469(1987)044<0542:AAITFT>2.0.CO;2.

Schubert, W. H., and J. J. Hack, 1982: Inertial stability and tropical cyclone development. *J. Atmos. Sci.*, **39**, 1687–1697, doi:10.1175/1520-0469(1982)039<1687:ISATCD>2.0.CO;2.

——, and ——, 1983: Transformed Eliassen balanced vortex model. *J. Atmos. Sci.*, **40**, 1571–1583, doi:10.1175/1520-0469(1983)040<1571:TEBVM>2.0.CO;2.

——, and B. T. Alworth, 1987: Evolution of potential vorticity in tropical cyclones. *Quart. J. Roy. Meteor. Soc.*, **113**, 147–162, doi:10.1002/qj.49711347509.

——, M. T. Montgomery, R. K. Taft, T. A. Guinn, S. R. Fulton, J. P. Kossin, and J. P. Edwards, 1999: Polygonal eyewalls, asymmetric eye contraction, and potential vorticity mixing in hurricanes. *J. Atmos. Sci.*, **56**, 1197–1223, doi:10.1175/1520-0469(1999)056<1197:PEAECA>2.0.CO;2.

Skamarock, W. C., and J. B. Klemp, 2008: A time-split nonhydrostatic atmospheric model for research and NWP applications. *J. Comput. Phys.*, **227**, 3465–3485, doi:10.1016/j.jcp.2007.01.037.

Smith, R. K., 1980: Tropical cyclone eye dynamics. *J. Atmos. Sci.*, **37**, 1227–1232, doi:10.1175/1520-0469(1980)037<1227:TCED>2.0.CO;2.

Stern, D. P., and F. Zhang, 2013a: How does the eye warm? Part I: A potential temperature budget analysis of an idealized tropical cyclone. *J. Atmos. Sci.*, **70**, 73–90, doi:10.1175/JAS-D-11-0329.1.

——, and ——, 2013b: How does the eye warm? Part II: Sensitivity to vertical wind shear and a trajectory analysis. *J. Atmos. Sci.*, **70**, 1849–1873, doi:10.1175/JAS-D-12-0258.1.

Stewart, S. R., 2014: Tropical cyclone report: Hurricane Edouard (AL062014). NOAA/National Hurricane Center Tech. Rep. AL062014, 19 pp., http://www.nhc.noaa.gov/data/tcr/AL062014_Edouard.pdf.

Tao, C., and H. Jiang, 2015: Distributions of shallow to very deep precipitation–convection in rapidly intensifying tropical cyclones. *J. Climate*, **28**, 8791–8824, doi:10.1175/JCLI-D-14-00448.1.

Weng, Y., and F. Zhang, 2016: Advances in convection-permitting tropical cyclone analysis and prediction through EnKF assimilation of reconnaissance aircraft observations. *J. Meteor. Soc. Japan*, **94**, 345–358, doi:10.2151/jmsj.2016-018.

Willoughby, H. E., J. A. Clos, and M. G. Shoreibah, 1982: Concentric eye walls, secondary wind maxima, and the evolution of the hurricane vortex. *J. Atmos. Sci.*, **39**, 395–411, doi:10.1175/1520-0469(1982)039<0395:CEWSWM>2.0.CO;2.

Xu, J., and Y. Wang, 2010: Sensitivity of tropical cyclone inner-core size and intensity to the radial distribution of surface entropy flux. *J. Atmos. Sci.*, **67**, 1831–1852, doi:10.1175/2010JAS3387.1.

Zagrodnik, J. P., and H. Jiang, 2014: Rainfall, convection, and latent heating distributions in rapidly intensifying tropical cyclones. *J. Atmos. Sci.*, **71**, 2789–2809, doi:10.1175/JAS-D-13-0314.1.

Zawislak, J., H. Jiang, G. R. Alvey III, E. Zipser, J. A. Zhang, and S. N. Stevenson, 2016: Observations of the structure and evolution of Hurricane Edouard (2014) during intensity change. Part I: Relationship between the thermodynamic structure and precipitation. *Mon. Wea. Rev.*, **144**, 3333–3353, doi:10.1175/MWR-D-16-0018.1.

Zhang, D.-L., and H. Chen, 2012: Importance of the upper-level warm core in the rapid intensification of a tropical cyclone. *Geophys. Res. Lett.*, **39**, L02806, doi:10.1029/2011GL050578.

Zhang, F., and D. Tao, 2013: Effects of vertical wind shear on the predictability of tropical cyclones. *J. Atmos. Sci.*, **70**, 975–983, doi:10.1175/JAS-D-12-0133.1.

——, and Y. Weng, 2015: Predicting hurricane intensity and associated hazards: A five-year real-time forecast experiment with assimilation of airborne Doppler radar observations. *Bull. Amer. Meteor. Soc.*, **96**, 25–32, doi:10.1175/BAMS-D-13-00231.1.

——, ——, J. A. Sippel, Z. Meng, and C. H. Bishop, 2009: Cloud-resolving hurricane initialization and prediction through assimilation of Doppler radar observations with an ensemble Kalman filter: Humberto (2007). *Mon. Wea. Rev.*, **137**, 2105–2125, doi:10.1175/2009MWR2645.1.

——, ——, J. F. Gamache, and F. D. Marks, 2011: Performance of convection permitting hurricane initialization and prediction during 2008–2010 with ensemble data assimilation of inner-core airborne Doppler radar observations. *Geophys. Res. Lett.*, **38**, L15810, doi:10.1029/2011GL048469.